

Image Analysis for Volumetric Characterisation of Microstructure

Maria Axelsson

*Centre for Image Analysis
Uppsala*

**Doctoral Thesis
Swedish University of Agricultural Sciences
Uppsala 2009**

Cover: Volume rendering of the estimated three-dimensional fibre orientation in a wood fibre composite. The fibres are coloured according to the estimated orientation.

ISSN 1652-6880

ISBN 978-91-86195-66-3

© Maria Axelsson 2009

Printed in Sweden by Universitetstryckeriet, Uppsala University, Uppsala, 2009

Abstract

Maria Axelsson. *Image Analysis for Volumetric Characterisation of Microstructure*.
Doctoral Thesis.

ISSN 1652-6880, ISBN 978-91-86195-66-3.

Digital image analysis provides methods for automatic, fast, and reproducible analysis of images. The main contribution of this thesis is new image analysis methods for volumetric characterisation of microstructure with application in the field of material science. The methods can be used as tools to characterise material microstructure, in particular the structure of fibre-based materials, such as paper, wood fibre composites, and press felts. More information about the material microstructure enables design of new materials with more specialised properties.

Volume images have recently become available to characterise material microstructure. Manual inspection of material properties using volume images is both non-reproducible and expensive. The methods presented in this thesis are developed to meet the growing need for automated analysis. The focus has been on 3D methods for high-resolution volume images, such as X-ray microtomography images.

New methods for characterisation of both the fibre structure and pore structure in fibre-based materials are presented. The fibre structure can be characterised by measuring either individual fibres or the local structure of the material. A method for tracking individual fibres in volume images is presented. The method is designed for wood fibres, but can also be applied to other types or fibres or in other areas where tubular or elongated structures are analysed in volume images. A method for estimating 3D fibre orientation of both tubular and solid fibres is also presented. Both methods have been evaluated on real volume images acquired using X-ray microtomography with good results. Two new pore structure representations and corresponding measurements are introduced. The usefulness of the methods is illustrated on real data. A method for estimating the pore volume at the interface between press felt and fibre web is presented. It has been applied in a case study of press felts under load using confocal microscopy images.

In addition to the methods for fibre-based materials, a general method for reducing ring artifacts in X-ray microtomography images is presented. The method is evaluated on real data with good results. It is also applied as a preprocessing step before further analysis of the X-ray microtomography images.

Keywords: image analysis, volume images, 3D, microstructure, segmentation, orientation, material characterisation, fibre, pore structure, X-ray microtomography

Author's address: Centre for Image Analysis, Box 337, SE-751 05 Uppsala, Sweden

Contents

1	Introduction	9
1.1	Outline of the thesis	9
2	Fibre-based materials	11
2.1	Paper	11
2.2	Wood fibre composite materials	12
2.3	Press felt	12
3	Imaging fibre-based materials	13
3.1	2D imaging	13
3.1.1	Light microscopy	13
3.1.2	Scanning electron microscopy	14
3.1.3	Confocal laser scanning microscopy	19
3.2	3D imaging	20
3.2.1	Slice based methods	20
3.2.2	X-ray microtomography	20
3.3	Comparison between different imaging devices	23
3.4	Visualising the 3D structure	27
4	Preprocessing	33
4.1	Ring artifact reduction	33
4.2	Noise reduction	37
5	Pore structure characterisation	41
5.1	3D Pore structure characterisation of paper	41
5.1.1	Binarisation	41
5.1.2	Finding the paper surface	42
5.1.3	Segmentation of individual pores	42
5.1.4	Individual pore based skeleton	45
5.1.5	Measurements on the pore structure	45
5.2	Estimation of the pore volume between paper and press felt	47
6	Fibre segmentation	51
7	Fibre orientation estimation	59
8	Conclusion and future work	67
8.1	Summary of contributions	67
8.2	Future work	68
	Related work	75
	Acknowledgments	77

List of enclosed papers

This thesis is based on the following papers, which are referred to by Roman numerals in the text. All published papers are reproduced with permission from the respective publisher.

- I Axelsson, M., Svensson, S., Borgefors, G. (2006). Reduction of Ring Artifacts in High Resolution X-Ray Microtomography Images. In K. Franke et al. (Eds.), *Proc. of 28th Annual Symposium of the German Association for Pattern Recognition, Berlin, Germany, Lecture Notes in Computer Science 4174*, Springer-Verlag, pp. 61–70.
- II Sintorn, I.-M., Svensson, S., Axelsson, M., Borgefors, G. (2005). Segmentation of individual pores in 3D paper images. *Nordic Pulp and Paper Research Journal*, 20(3):316–319.
- III Axelsson, M., Svensson, S. (2009). 3D pore structure characterisation of paper. *Accepted for publication in Pattern Analysis and Applications*.
- IV Axelsson, M., Östlund, C., Vomhoff, H., Svensson, S. (2006). Estimation of the pore volume at the interface between paper web and press felt. *Nordic Pulp and Paper Research Journal*, 21(3):395–402.
- V Axelsson, M. (2007). 3D Tracking of Cellulose Fibres in Volume Images. In *Proc. of 14th International Conference on Image Processing*, San Antonio, Texas, USA, pp. IV 309–312.
- VI Axelsson, M. (2008). Estimating 3D Fibre Orientation in Volume Images. In *Proc. of 19th International Conference on Pattern Recognition*, Tampa, Florida, USA.
- VII Axelsson, M. (2009). An evaluation of scale and noise sensitivity of fibre orientation estimation in volume images. *Submitted for publication*.

1 Introduction

The availability of high resolution three-dimensional (3D) imaging devices is increasing and volume images are more frequently used in characterisation of material microstructure. The amount of data that needs to be processed in a single volume image is large, which makes manual inspection of the volume images both time consuming and expensive. In addition, results from manual inspection are often non-reproducible. Volume images can be efficiently processed and analysed without manual inspection using digital image analysis.

This thesis presents new image analysis methods for characterisation of microstructure of fibre-based materials using high resolution volume images. The focus of the research has been to develop fully automated 3D segmentation and analysis methods for both fibres and pores in volume images of fibre-based materials, in particular for paper, wood fibre composites, and press felts. Most fibre-based materials are designed to have specific structural properties. They are state of the art and well suited for their respective applications. However, little is known about the 3D microstructure of many of our most common materials. The main objective of this thesis is to present new image analysis tools that can be used to increase the knowledge about the relationship between the 3D microstructure and the macroscopic properties of fibre-based materials. This knowledge enables design of new materials with more specialised properties.

The work has been focused on 3D methods which utilise more of the available information in the volume images than in previous methods. It has also been focused on development of methods suitable to analyse large amounts of data. The methods are developed to meet the growing need for automated analysis in the field of material science. They are developed in collaboration with paper scientists and other material experts. The methods that are presented in this thesis for analysis of fibre-based materials are new methods for pore structure characterisation of paper, estimation of the interface volume between paper and press felt, individual fibre tracking, and fibre orientation estimation. The methods are general and can also be applied to segment and characterise other porous, elongated, or tubular structures, for example in medical applications. In addition, a general method for ring artifact reduction is presented. The contributions of this thesis aim at fully automatic analysis of the microstructure of fibre-based materials, where any desired structure measurement is available.

1.1 Outline of the thesis

The outline of the thesis is as follows:

- Chapter 2 contains a brief description of the fibre-based materials that have been used during the development of the presented methods.
- Chapter 3 presents an overview of the available imaging techniques for acquiring 2D and 3D images of the microstructure of fibre-based materials. Five

different imaging devices for 3D imaging of paper are compared and the microstructure of some example materials is illustrated in 2D and 3D.

- Chapter 4 describes the preprocessing steps that must be applied to the volume images before they can be analysed. This chapter presents the first contribution of this work: a method for ring artifact reduction of X-ray microtomography images (Paper I).
- Chapter 5 presents methods for pore structure characterisation of paper using volume images (Paper II and Paper III) and a method for estimating the interface pore volume between paper and press felt using confocal images of press felt (Paper IV).
- Chapter 6 presents a method for fibre tracking in volume images intended for segmentation of individual fibres (Paper V).
- Chapter 7 presents a method for estimating fibre orientation in volume images (Paper VI and Paper VII).
- Chapter 8 concludes the thesis with a summary of the scientific contributions and suggestions for future work.

2 Fibre-based materials

There are many different types of fibre-based materials. Some examples are glass fibre reinforced plastics, carbon fibre reinforced plastics, paper, wood fibre composites, textiles, and felts. The methods in this thesis are developed mainly for materials based on wood fibres, such as paper and wood fibre composites, and for press felts. These materials are briefly described in this chapter. Their microstructure is illustrated in Chapter 3.

2.1 Paper

Paper is used in many areas of our everyday life. Some important applications are transportation and protection of goods (bags, sacks, and packaging), communicating and storing information (newspaper, books, and copy paper), and personal hygiene (tissues and napkins). Papermaking is a big industry, especially in the Nordic countries where the raw material is abundant.

Papermaking has been around for a long time. Already the ancient Egyptians used papyrus to make writing material around 3500 BC. In 105 AD the Chinese made paper from rags and other fibres, using the first known method for pulping. This technology spread westwards and paper was produced in Europe in the early 12th century. The usage of wood in papermaking is a more recent innovation that began with mechanical pulping in the 1840s. The breakthrough innovation in papermaking was the Fourdrinier machine that was patented in 1799. It takes pulp as input and outputs a final paper product. Today, paper machines follow the general layout of this machine with a wet end, press section, dryer section, and calender section.

In the wet end the pulp is distributed from the headbox of the machine onto a wide screen, the wire, which moves with high speed. The direction in which the wire moves is called the Machine Direction (MD). Paper produced in a paper machine always has more fibres oriented in this direction due to the high speed and flow in the machine. The direction across the machine is called the Cross Machine Direction (CMD) and the direction out of the paper plane is called the Z-direction.

The water content is reduced in a number of steps after the fibre network has been formed on the wire. First, vacuum is used in the wet end, then press felts and press rolls are used in the press section, and last steam-heated rollers are used in the dryer section. After the dryer section the paper can also be calendered or coated to make the surface smoother using heated rollers.

The fibres are bound together by hydrogen bonds. The surface of the fibres is often roughened by beating the fibres in a refinement step. This increases the area with available hydroxyl groups that can form bonds, and consequently makes the paper stronger. However, too much refinement makes the fibres weaker and the strength decreases again.

The final product is a complex 3D fibre network which is highly porous. Both the fibre network and the pore structure govern important material properties. The

fibre orientation and the amount of fibre-fibre bonds in the fibre network determine, for example, strength and stiffness and the pore structure determines, for example, print and transport properties. The structure is designed to fit the specific needs for each application using different wood fibre types, pulping methods, filling materials, forming methods, or other process parameters.

2.2 Wood fibre composite materials

In wood fibre composite materials, wood fibres are used as reinforcement of polymers. The base material, the matrix, is reinforced to improve properties such as stiffness and strength. Wood fibre composites have many potential uses in new applications, for example, in automotive applications or in the building sector. As the materials improve, new application areas become available.

The properties of wood fibre composite materials depend on the microstructure of both the matrix and the reinforcement material. It is important to characterise the stress transfer properties of the matrix-fibre interface and properties such as fibre orientation to be able to design new materials with improved properties.

2.3 Press felt

Press felts are used in the production of paper to press out water from the wet fibre web in a series of press nips. This process takes place in the press section and is called wet pressing. Some water is sucked back into the paper after the press nip. However, mechanical pressing is still far more efficient than drying the web directly after the forming step in the wet end.

Press felts consist of synthetic fibres of different sizes. The fibres are usually made of polyamide. The largest fibres form the base weave, which is a woven regular network. Batt fibres with smaller diameter are needled onto this structure using fibres with even smaller diameter. The batt fibres create a porous structure on each side of the base weave. The microstructure of the press felt, in particular the pore structure, is important, since it determines the water holding capacity. This, in turn, determines the efficiency of the dewatering. The structure is designed for different dewatering situations, to remove large or small amounts of water. Increased knowledge about the microstructure of the felt under compression is important in the design of new felts.

3 Imaging fibre-based materials

Microscopy techniques can be used to gain information about the microstructure of a material. This chapter presents an overview of the available techniques to acquire 2D and 3D images of paper and other fibre-based materials. Five different imaging devices for imaging volume images of paper are compared. The microstructure of different fibre-based materials is illustrated using 3D surface renderings.

In structure analysis of paper, both the surface structure and the internal structure are important. For wood fibre composites the internal structure is most interesting. High resolution microscopy techniques are needed to resolve individual wood fibres. Wood fibres are long tubular structures. The void interior is called lumen. Softwood fibres have diameters of 30–50 μm and are 3–5 mm long and hardwood fibres have diameters of 10–20 μm and are 1–3 mm long. A resolution below 1 μm is preferable for measurements of individual fibre properties. When analysing volume images, this high resolution adds to storage, memory, and processing time requirements, since large images must be acquired to gather information about a representative part of the material. Even higher resolution is needed to characterise small pores that influence, for example, print quality. For other measurements it is possible to obtain good estimates using lower resolution. See, for example, the 3D fibre orientation estimation in Chapter 7. The desired structure measurement determines which imaging technique that is most suitable for the analysis.

3.1 2D imaging

Fibre-based materials such as paper, wood fibre composites, and press felts can be imaged in 2D using light microscopy, scanning electron microscopy, and confocal laser scanning microscopy. Each of these imaging techniques can provide high resolution images of the surface or of the internal structure in cross sections of materials and are commonly used to characterise the 2D structure. The following sections describe these modalities briefly.

Cross sectional images can be used to measure many material properties. However, the materials often have a large structure variation and the local structure may not be representative. Often, many 2D images must be acquired to obtain good statistics. For paper, 2D images provide measurements on paper cross sections such as the material density distribution in the Z-direction or the coating layer thickness.

3.1.1 Light microscopy

In a Light Microscope (LM) 2D images are acquired using visible light. It is common to use a digital camera as detector to capture a 2D image directly. Thin slices of the material can be imaged using a number of microscopy techniques, such as bright field, phase contrast, and fluorescence. The LM is suited to view the surface or cross sections of paper samples. Cross sections are imaged by embedding the sample in epoxy resin and cutting slices with a thickness of about 1 μm using a microtome. There are often problems with cutting artifacts or geometric distortions caused by the sample preparation. The samples are stained to increase contrast in

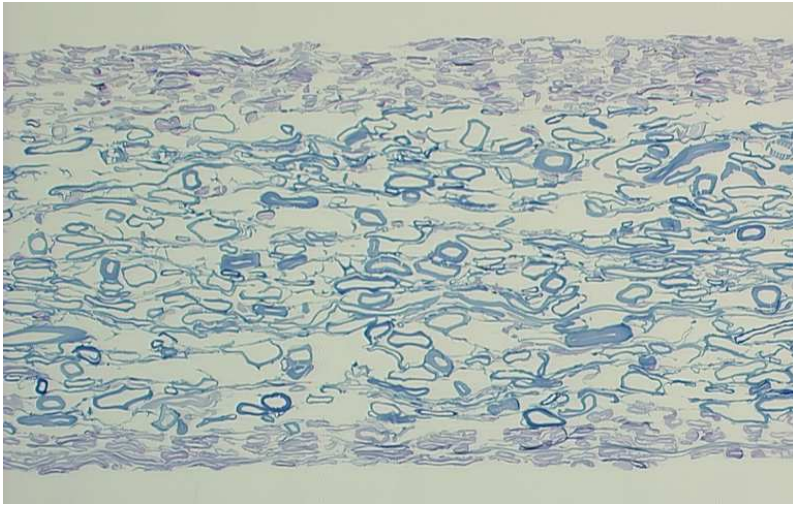


Figure 1: LM image of a three layered cardboard. (The image was provided by STFI-Packforsk, Stockholm, Sweden.)

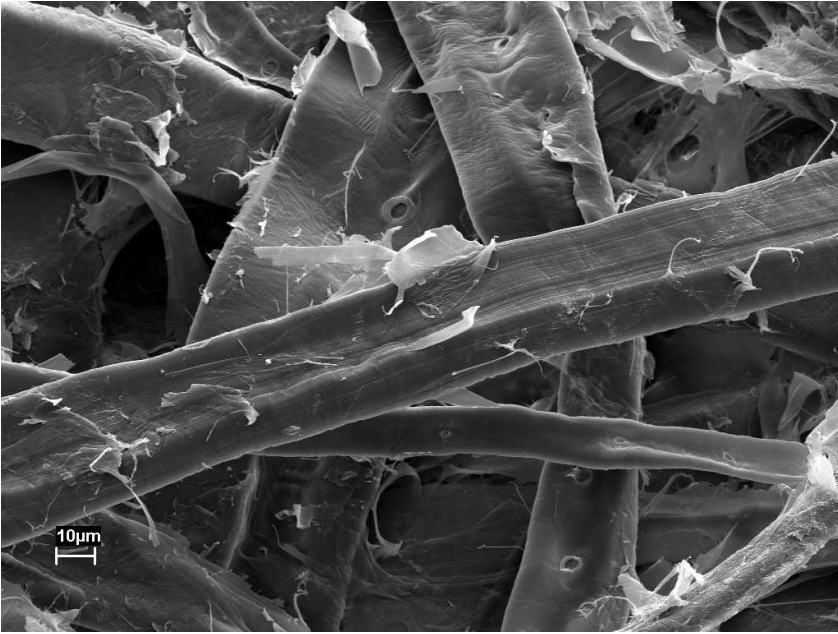
the images. Figure 1 shows an example of a three layered cardboard imaged in a LM using 10x magnification. The sample consists of chemical pulp and mechanical pulp. The dye used in the staining is absorbed to a greater degree by the mechanical pulp in the central part of the cardboard.

3.1.2 Scanning electron microscopy

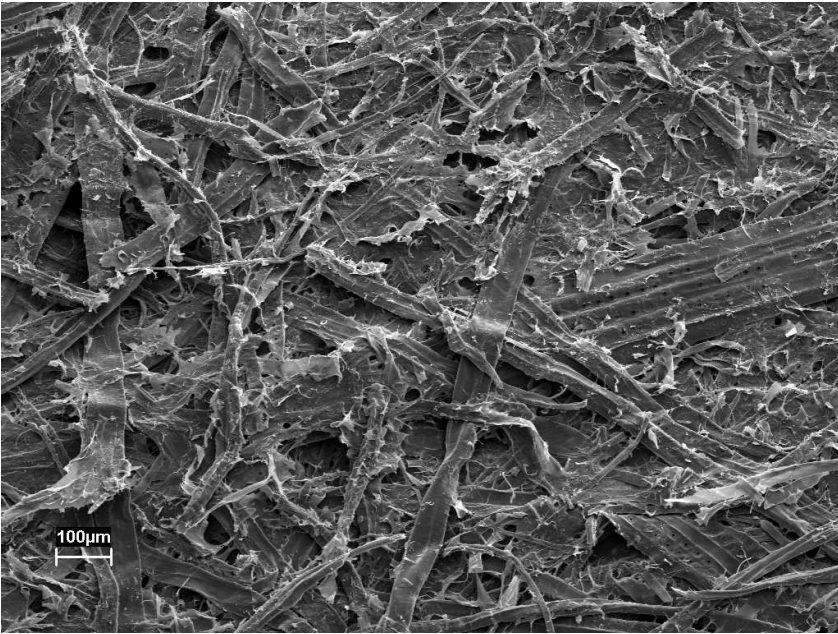
In a Scanning Electron Microscope (SEM) 2D images are collected by raster scanning the surface of the sample with a focused electron beam. The collected signal can provide information about the topography of the surface, the material density, or other properties. When imaging paper it is usually the signal from the so called secondary electrons that is collected. The SEM has a large depth of field which gives the imaged structure a 3D appearance. See for example Figure 2(a) that shows details of wood fibres. Note the small holes in the fibres that are used for fluid transport in the wood. Figure 2(b) shows an overview of the more porous middle section of a layered cardboard after freezing the sample and splitting it open.

The surface of different paper grades can easily be imaged directly or after applying a gold coating. To image the internal structure of paper, it is common to embed the material in epoxy resin and image polished cross sections (Walbaum and Zak, 1976). Since the material needs to be sliced to image the internal structure, there are sometimes cutting artifacts. Figure 8 shows an example of a SEM image of a paper cross section.

Figure 3 and 4 show example images of the surface of different paper grades. The difference in surface structure is clearly visible in the images. Figure 5 illustrates laser print on copy paper. The paper structure, in particular the paper surface, is important in printing applications.

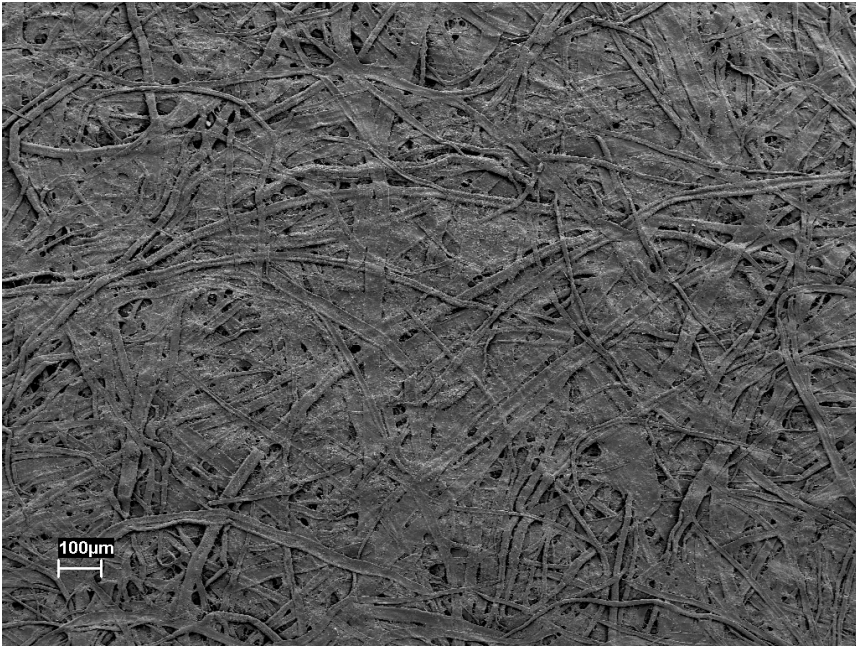


(a)

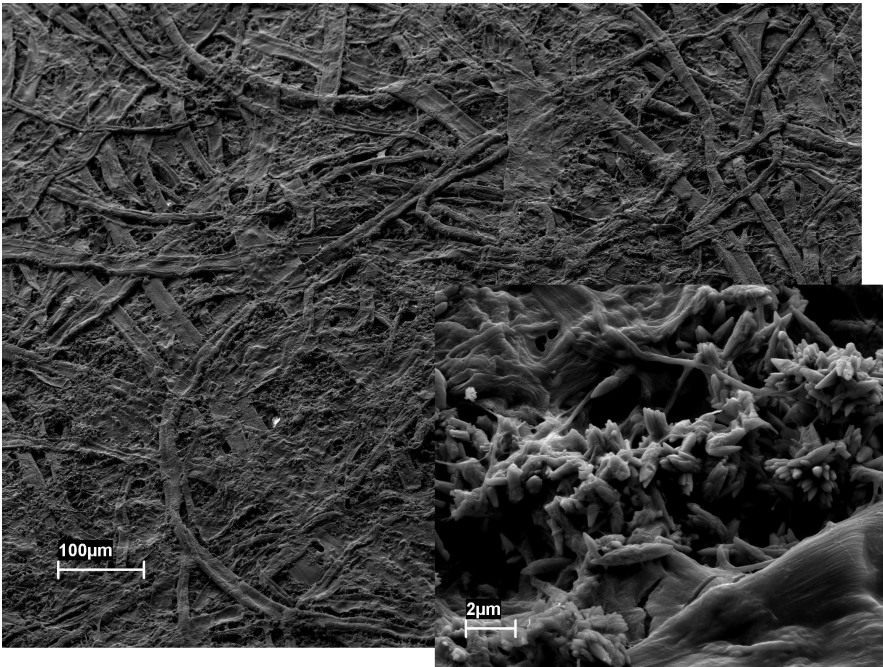


(b)

Figure 2: SEM images showing the middle section of a layered cardboard. (a) Detail of wood fibres. (b) Overview of the fibre structure.



(a)



(b)

Figure 3: SEM images showing the surface structure of two paper grades. (a) Cardboard. (b) Copy paper with detail of the filling material.

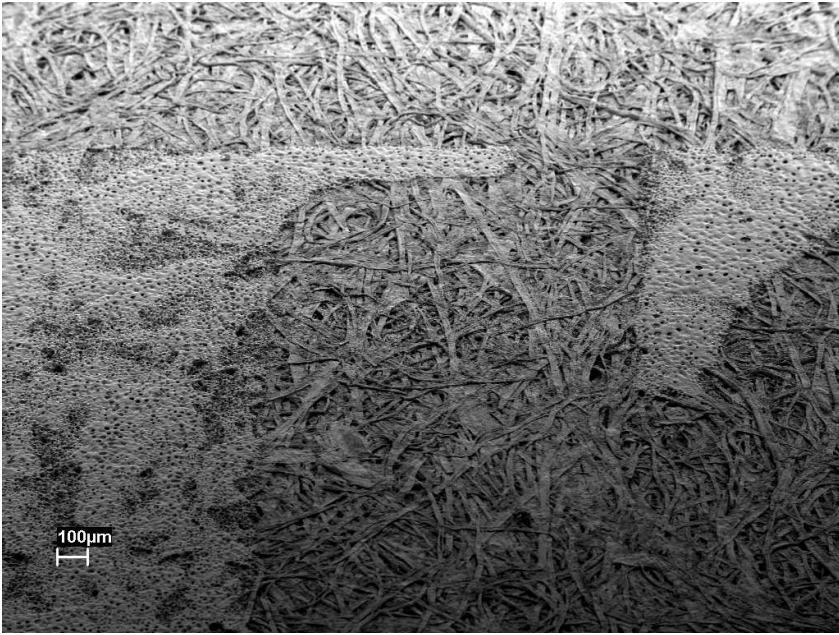


(a)

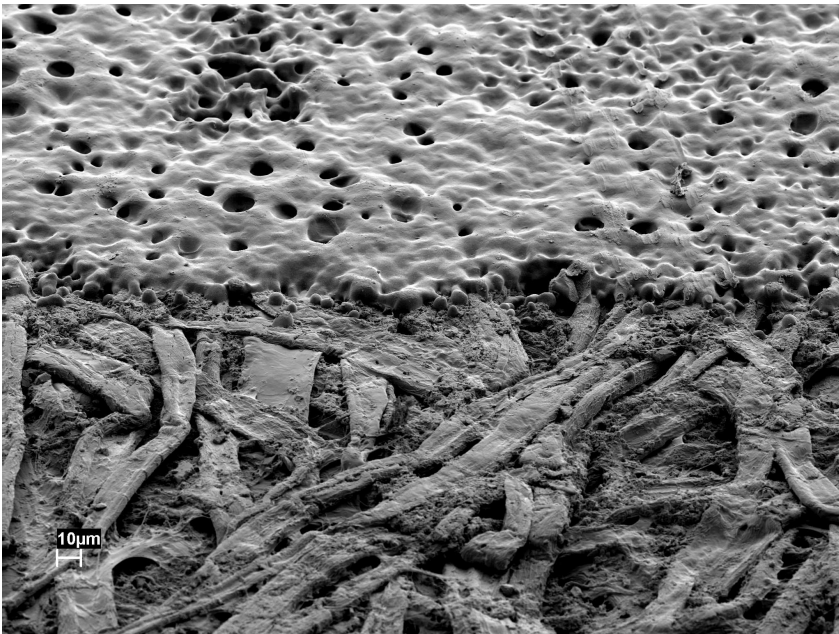


(b)

Figure 4: SEM images showing the surface structure of two paper grades. (a) Coffee filter. (b) Tissue (toilet paper).



(a)



(b)

Figure 5: SEM images showing print from a laser printer on copy paper. (a) Detail of the serifs for the letters IT. (b) Detail of the print on the paper surface.

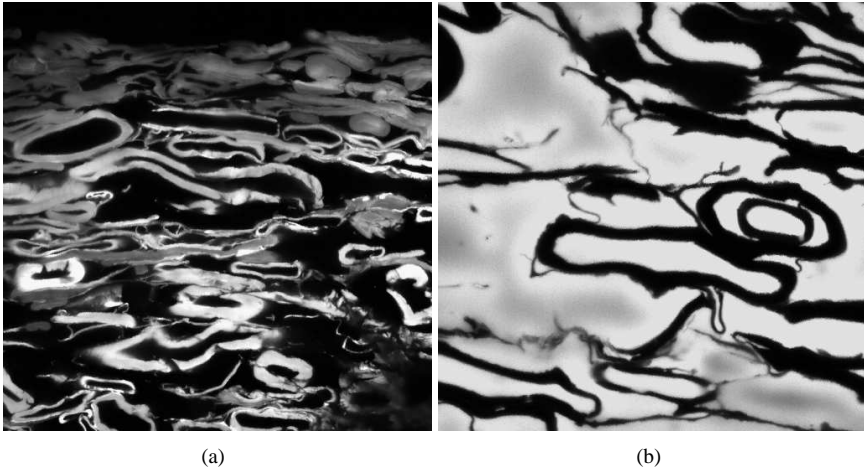


Figure 6: CLSM images showing cross sections of a layered cardboard embedded in epoxy resin. (a) Sample with stained fibres. (b) Sample with stained epoxy resin, which gives an image with negative contrast.

3.1.3 Confocal laser scanning microscopy

In a Confocal Laser Scanning Microscope (CLSM) 2D images are collected by raster scanning the sample with a focused laser beam. The collected signal is fluorescent light emitted from the sample at the point that is excited by the laser. Normally, the sample is stained with fluorochrome dye to increase the fluorescent signal.

The CLSM can provide volume images of samples using optical sectioning by focusing on points at different depths in the sample. However, this technique is not very effective for wood fibres, since the attenuation of the light is rapid in the material. Only the surface of the sample can be imaged with good quality. The CLSM is commonly used to image the surface and cross sections of paper (Moss et al., 1993; Dickson, 2000). For embedded samples, the focus can be set just below the surface of the embedding to reduce the impact of cutting artifacts in the images.

Figure 6 shows two example images of paper cross sections. The samples were embedded in epoxy resin and polished. In Figure 6(a) the fibre network is stained and imaged using a 63x oil immersion objective with a voxel size of $0.31\ \mu\text{m}$ parallel to the objective and $0.12\ \mu\text{m}$ in the depth direction. The staining varies between the different layers of the cardboard, since they consist of different pulp types. The fluorescent signal from the less stained pulp type is weaker, which makes it difficult to obtain optimal contrast everywhere by adjusting the intensity of the incoming light. In Figure 6(b) the epoxy resin is stained to create negative contrast. The sample is imaged using a 100x oil immersion objective with a voxel size of $0.20\ \mu\text{m}$ parallel to the objective and $0.20\ \mu\text{m}$ in the depth direction.

3.2 3D imaging

None of the imaging devices described in Section 3.1 can directly provide volume images suitable for 3D microstructure characterisation. Two approaches have been used to image paper and other fibre-based materials in 3D. One approach is slice based methods, where successive cuts of the material are imaged and registered to a volume image. Another approach is X-ray microtomography, which provides volume images by non-destructive scanning of the material.

3.2.1 Slice based methods

The first reconstruction of a volume image of paper using a slice based method was presented by Hasuike et al. (1992). A paper sample was embedded in epoxy resin and sliced using a microtome. The cut-off slices were imaged in a differential interference microscope. Aronsson et al. (2002) reconstructed a volume image of a five layered cardboard embedded in epoxy. The surface of the embedding was imaged using SEM and a slice of the embedding was cut off using a microtome between successive images. Imaging the embedding instead of the cut-off slices reduced cutting artifacts in the images. Another slicing method was presented by Wiltche (2005) where the sample was both sliced using a microtome and imaged directly using a light microscope in an automated process. An alternative to microtome slicing is controlled serial grinding. Chinga et al. (2004) presented a method where the grinding depth can be determined by adding mono-disperse beads close to the paper surface. An advantage of the slice based methods is that the imaging devices are common in regular labs. The volumes produced by the slice based methods often have non-cubic voxels, since the resolution usually is higher in the collected 2D images than the step length between successive slices. It is also time consuming to collect the images and there are problems with registration, cutting artifacts, and uneven staining in the reconstruction and analysis of the volumes.

3.2.2 X-ray microtomography

Volume images can be obtained without physical sectioning using X-ray microtomography. The technique is the same as for Computed Tomography (CT) devices used for medical applications, but the voxel size is in the micrometer range.

The sample is placed in an X-ray beam and the attenuation of the beam is captured on a 2D detector array. The registered pixel value is the attenuation of the incoming beam along a ray through the sample. The attenuation can be described as

$$I = I_0 \exp\left(-\int \mu(x, y, z) ds\right) \quad (1)$$

where I is the recorded pixel value, I_0 is the incoming beam intensity and $\mu(x, y, z)$ is the attenuation coefficient. The sample is rotated over 180 degrees and 2D projections are captured at approximately 1200 positions. A volume image can be reconstructed from the projections using, for example, filtered back projection (Bracewell and Riddle, 1967).

There are two main types of microtomography devices available; synchrotron radiation X-ray microtomographs and desktop X-ray microtomographs. Synchrotrons can produce a high intensity, monochromatic parallel beam, which provides high resolution images that are suitable for detailed structure characterisation of wood fibre-based materials (Samuelsen et al., 2001). Desktop X-ray microtomography scanners, such as Skyscan¹ or Xradia² devices, can produce a lower intensity, polychromatic fan beam, which provides images with lower resolution (Goel et al., 2001; Huang et al., 2002). Both types of imaging devices are constantly improving and in recent years desktop scanners have become more common.

There are no cutting artifacts in X-ray microtomography images, since the imaging method is non-destructive. Also, the voxels are cubic and the contrast is even throughout the volume. However, there are other deficits in X-ray microtomography images. As for all measured images, noise is always present in the images, since the available integration time for the detected signal is limited. Another problem in tomography and other rotating imaging techniques is ring artifacts, which is further described in Chapter 4.

Typical reconstructed volumes are $1024 \times 1024 \times 1024$ voxels or $2048 \times 2048 \times 2048$ voxels with 8, 16, or 32 bit precision. The Field of View (FoV) is a cylinder, due to the rotation during the scan. At synchrotron facilities a common diameter is 1.4 mm for the FoV, when using a voxel size of $0.7 \mu\text{m}$ and a detector width of 2048 pixels. If the full height is used for a 2048×2048 pixel detector the cylinder height is 1.4 mm for the same resolution. If the samples fit into FoV, the Hounsfield scale can be used for comparing the absolute values between the volume images. Only the sample width is restricted to fit into the FoV for optimal contrast. If a large part of the sample is outside the FoV it is called local tomography. This data can also be analysed, but contrast and absolute image values may change considerably between images.

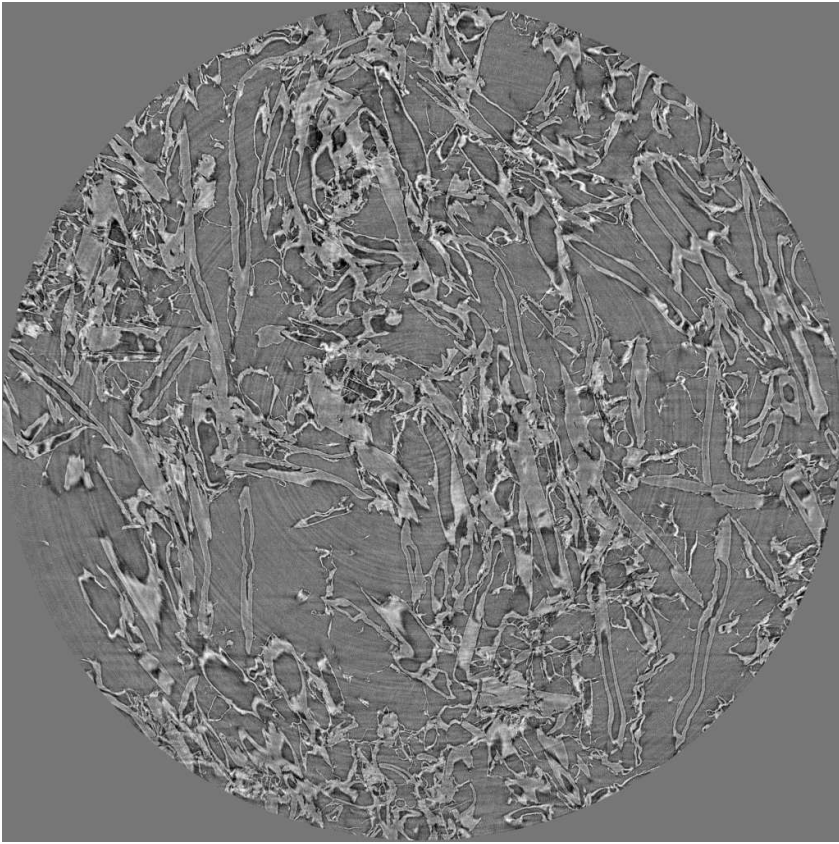
As the sample rotates during the acquisition the samples must be fixed to the sample holder. This introduces a problem for paper, since adhesives can change the structure. Post-it notes have been used since their glue does not penetrate the paper structure. However, the glue and wood fibres have similar density, which results in poor contrast between them. Developing automatic methods for removing the glue has proven to be difficult. This is not a problem for wood fibre composite materials, since only the internal structure is of interest.

Figure 7 shows two slices from an X-ray microtomography image. The slice in (a) is perpendicular to the rotation axis of the sample and shows the circular cross section of the FoV. The slice in (b) is perpendicular to the slice in (a) and shows the sample, the sample holder, and the fixture.

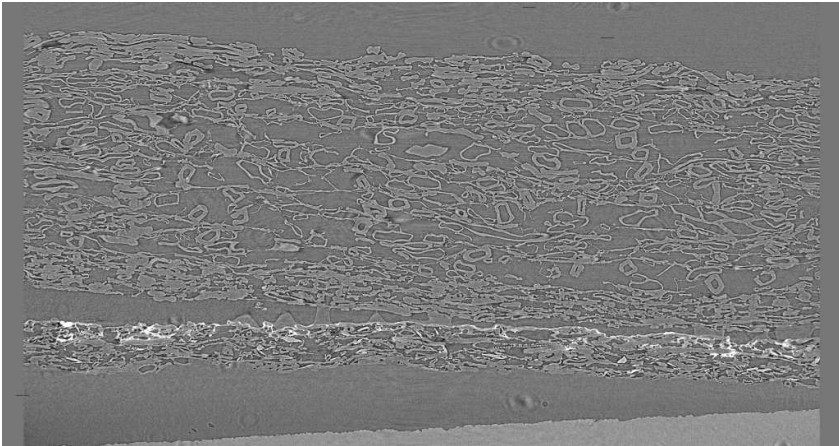
Different modes are available in X-ray microtomography. In absorption mode the densities of the sample are directly imaged using beam absorption (Rolland du Roscoat et al., 2005a). In phase contrast mode the sample-to-detector distance is increased. This gives an edge enhancement of the interface between different den-

¹Skyscan: <http://www.skyscan.be/>

²Xradia: <http://www.xradia.com/>



(a)



(b)

Figure 7: X-ray microtomography image of a cardboard sample. (a) A slice perpendicular to the rotation axis of the sample. The slice is 2048×2048 pixels. (b) A slice perpendicular to the slice in (a).

Table 1: Comparison of the voxel sizes and image sizes for five imaging devices used to image paper in 3D.

Imaging device	Beamline	Voxel size		Image size (voxels)
		XY (μm)	Z (μm)	
SEM	-	0.7	5	$3072 \times 768 \times 102$
Skyscan 1172	-	0.78	0.78	$1900 \times 1800 \times 870$
ESRF	ID 19	0.70	0.70	$2048 \times 2048 \times 2048$
PSI	Tomcat	0.70	0.70	$2048 \times 2048 \times 1024$
HASYLAB	BW2	1.44	1.44	$1135 \times 1135 \times 1022$

sities (Samuelsen et al., 2001; Antoine et al., 2002). Both phase contrast and absorption contrast may be present in the same image, see for example Figure 7. The phase contrast is visible as bright and dark voxels at the interface between fibre and void. It is also possible to obtain other types of phase contrast using different reconstruction methods.

3.3 Comparison between different imaging devices

In this section, a comparison between SEM and four different X-ray microtomography setups is presented. The same type of five layered cardboard (duplex board) was imaged in all devices, which makes the images directly comparable. The structure of the middle layers of the cardboard and the surface as seen by SEM are shown in Figure 2 and Figure 3(a), respectively.

The SEM volume used in the comparison is the sample acquired by Aronsson et al. (2002); Aronsson (2002b). The X-ray microtomography images were acquired on beamline ID 19 at European Synchrotron Radiation Facility (ESRF) in Grenoble, on beamline Tomcat at Paul Scherrer Institut (PSI) in Villigen, on beamline BW2 at Hamburger Synchrotronstrahlungslabor (HASYLAB) at the Deutsches Elektronen-Synchrotron (DESY) in Hamburg, and using a Skyscan 1172 at the Department of Physics at the University of Jyväskylä.

Each of the imaging devices can be used to image other materials or samples using different parameters. Here, the imaging parameters were optimised for paper to image as large part of the material as possible with a resolution sufficient to characterise the individual fibres and fibre cross sections. Table 1 shows the voxel sizes and image sizes for the imaging devices used in the comparison. All volumes were imaged using the largest possible FoV for the given resolution. In the imaging of the SEM volume, multiple images were captured between the successive microtome cuts to enlarge the FoV of the microscope.

Figure 8 shows a part of a slice from the reconstructed SEM volume and a 200×200 pixel detail of the slice. Figure 9 shows slices from the four X-ray microtomography images and a 200×200 pixel detail of each slice. Note that the images in the figures are cropped to show only the parts which contain the sample. The X-ray microtomography images from ESRF and PSI have high resolution in all dimensions,

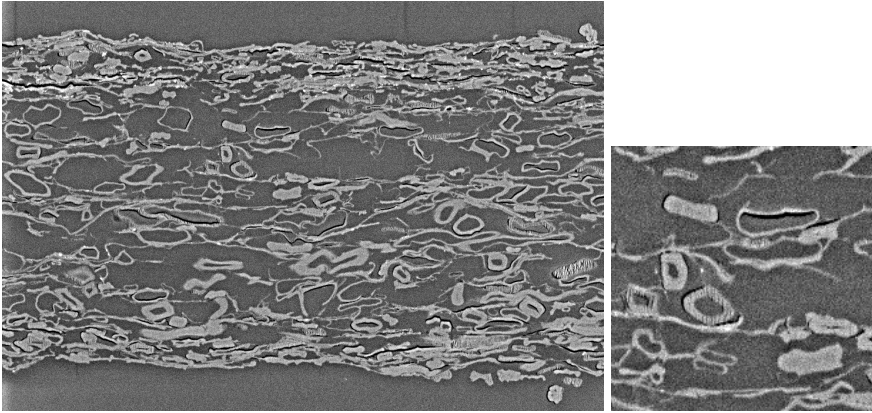


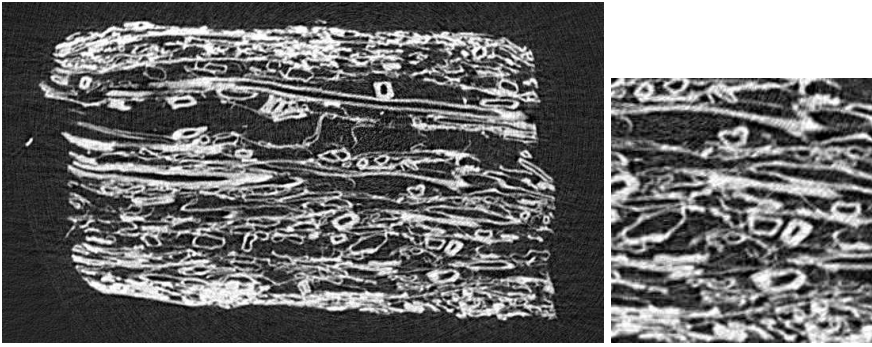
Figure 8: Image from a SEM volume of a layered cardboard and a 200×200 pixel detail of the image.

the SEM volume has high resolution in two of the three dimensions, and the other volumes have lower resolution. The volume from ESRF contains both absorption contrast and phase contrast. This effect is not as visible in the volumes from the other X-ray microtomography devices.

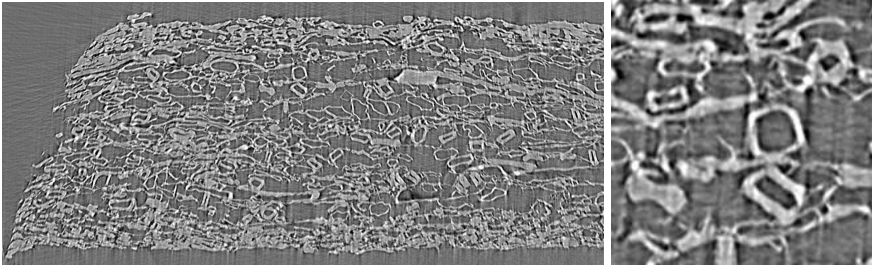
Figure 10 shows the histograms for the central part of the five volume images. The minimum and maximum values are not shown in the figure since the image intensities are clipped to 8 or 16 bits. The SEM volume and the volume from PSI have the best separation between fibre and void of the three high resolution volumes. The lower resolution volume from HASYLAB also has good separation between fibre and void.

The voxel size is cubic for the X-ray microtomography images and non-cubic for the SEM volume. Most conventional image analysis methods are designed for cubic voxels, which means that either the methods have to be adapted to non-cubic voxels or the volume has to be interpolated to cubic voxels.

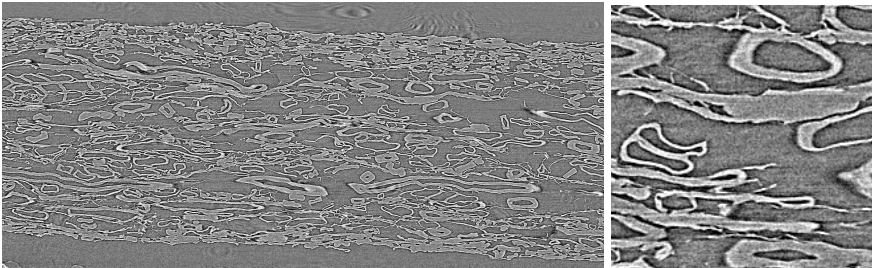
The SEM volume is the most time consuming volume to acquire. First the sample needs to be prepared by embedding it in epoxy resin. Then the sample is moved between the microtome and the SEM between each imaging step. As the imaging in the SEM requires vacuum, additional time is added to mount and unmount the sample. The scanning time for the X-ray microtomography devices depends on the scanning parameters. Parameters such as integration time, number of scanning steps, size of the FoV, and number of correction images determine the final scanning time. The scanning time was about 20 minutes for the sample imaged at ESRF ID 19, 30 minutes for the sample imaged at PSI Tomcat, a couple of hours for the sample imaged at HASYLAB BW2, and 8 hours for the sample imaged using the Skyscan 1172. The samples also need to be reconstructed. This can usually be done using batch jobs in parallel to the imaging and does not affect the required beam time. Sample preparation is straightforward for the X-ray microtomography images. The sample is placed in an environment with the same temperature and



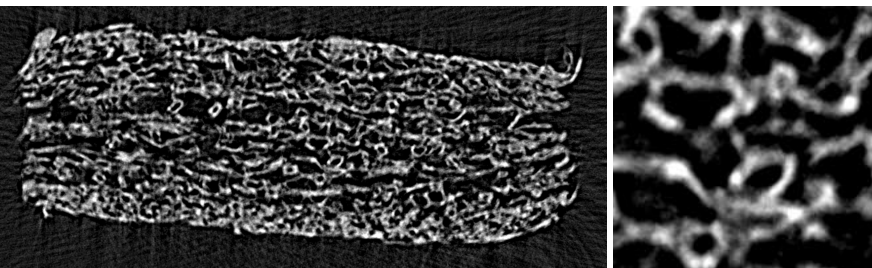
(a)



(b)



(c)



(d)

Figure 9: Images from four X-ray microtomography images of a layered cardboard with a 200×200 pixel detail of each image. (a) HASYLAB BW2 (b) PSI Tomcat (c) ESRF ID19 (d) Skyscan 1172

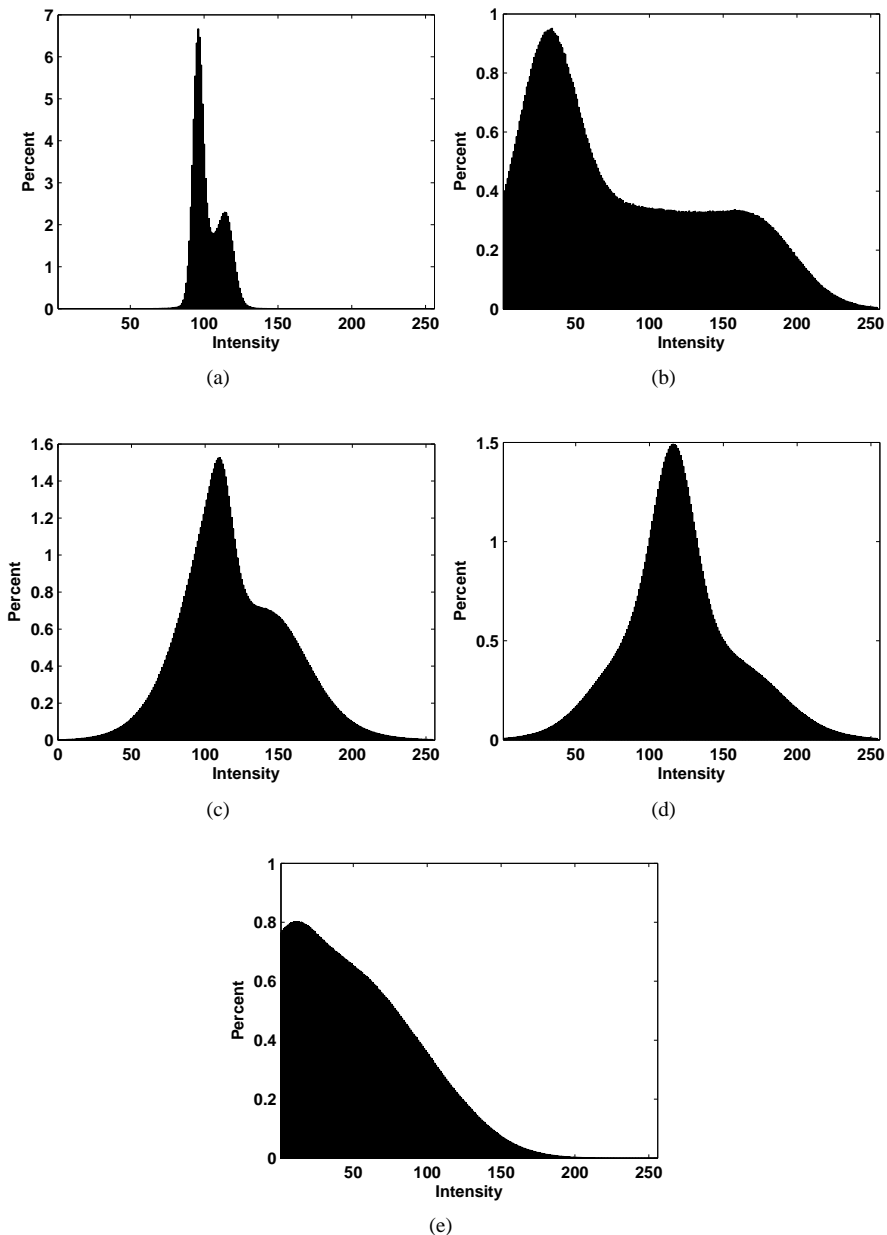


Figure 10: Histograms for the five volume images. (a) SEM volume (b) HASYLAB BW2 (c) PSI Tomcat (d) ESRF ID19 (e) Skyscan 1172

relative humidity as in the scanner before the image is acquired to avoid structure changes during the scan. The sample is mounted on a sample holder using glue or other adhesives. No embedding is required. As stated before, the X-ray microtomography imaging is non-destructive. This enables repeated scanning of the same sample under different conditions such as varying compression and moisture.

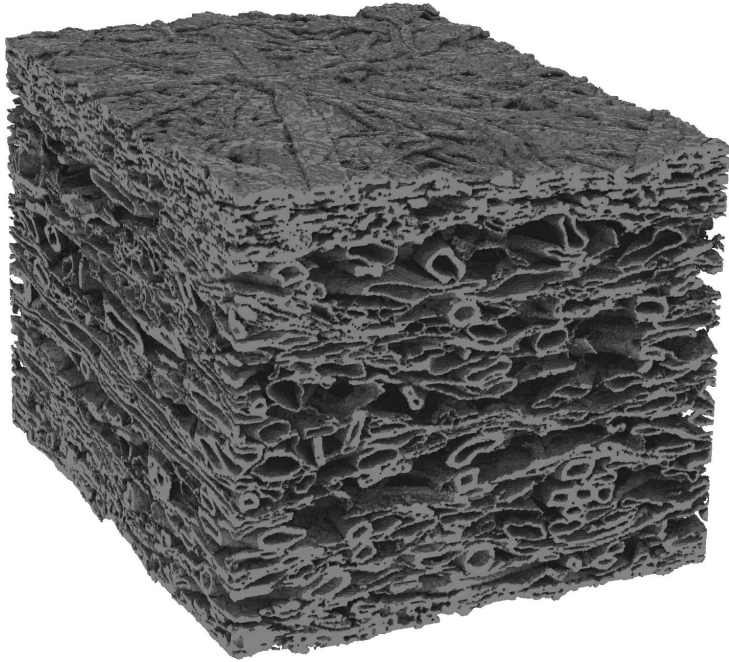
The required resolution depends on the desired measurements. Desktop scanners are more common and provide sufficient resolution for many measurements. For such measurements it is not necessary to spend valuable beam time at the synchrotron facilities. Synchrotron X-ray microtomography scanners provide high resolution images suitable for characterising details of individual fibres.

3.4 Visualising the 3D structure

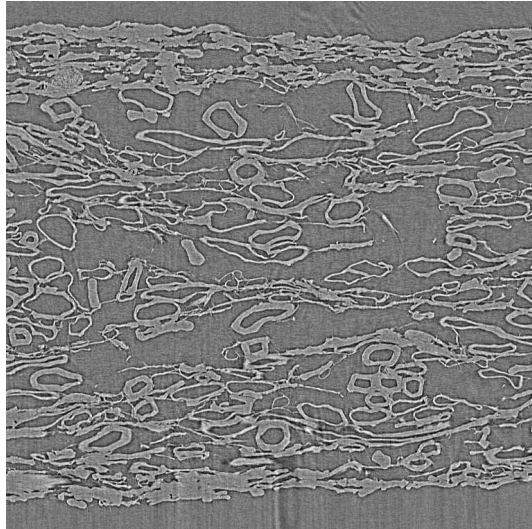
Visualisation is important for understanding the 3D structure. This section describes how volume images of fibre-based materials can be visualised and some example structures are illustrated. The visualised volumes are X-ray microtomography images from the ESRF beamline ID19, the PSI beamline Tomcat, and a Skyscan 1172 desktop scanner. The voxel size is $0.7 \times 0.7 \times 0.7 \mu\text{m}$ for the synchrotron volumes and $3.2 \times 3.2 \times 3.2 \mu\text{m}$ for the Skyscan volume. The volumes are preprocessed and binarised according to Section 4 and 5.1.1. The binary volume images are converted to 3D meshes using marching cubes, as presented by Lorensen and Cline (1987), using The Visualization Toolkit.³ The samples are surface rendered using ambient occlusion shading, presented by Landis (2002). Ambient occlusion makes the rendered objects appear as if it were a cloudy day. The appearance is similar to SEM images, which facilitates interpretation and comparison of the images.

Figure 11 shows the 3D structure of the same type of five layered cardboard that was used in the comparison between the imaging devices in Section 3.3. In the figure, the layered structure of the cardboard is clearly visible. The top and bottom layers are denser than the middle part. Figure 12 shows the 3D structure of a newsprint sample. Newsprint is a thin 3D structure with strongly oriented fibres for strength in the machine direction. The surface is rather rough, which puts a limit on the print sharpness. There is a large amount of fine material that gives high light scattering and thus high opacity. Figure 13 shows the 3D structure of a wood fibre composite material with an epoxy vinyl ester matrix and lab made softwood Kraft fibre. The matrix is made transparent in the surface rendering. The cardboard, the newsprint, and the composite material were imaged at the ESRF beamline ID 19. Some wood fibre composite materials are not as dense as the paper materials. However, the fibre networks are still complex. Figure 14 shows a wood fibre composite material based on a polypropylene matrix where the fibres have been pelletised before they are mixed with the matrix. Also in this case the matrix is made transparent in the surface rendering. The composite material was imaged at PSI beamline Tomcat. Figure 15 shows the 3D structure of a press felt. Note the layered structure with large fibres in the base weave and smaller batt fibres on each side. The volume image was acquired using a Skyscan 1172 at Albany International AB in Halmstad.

³The Visualization Toolkit: <http://www.vtk.org/>

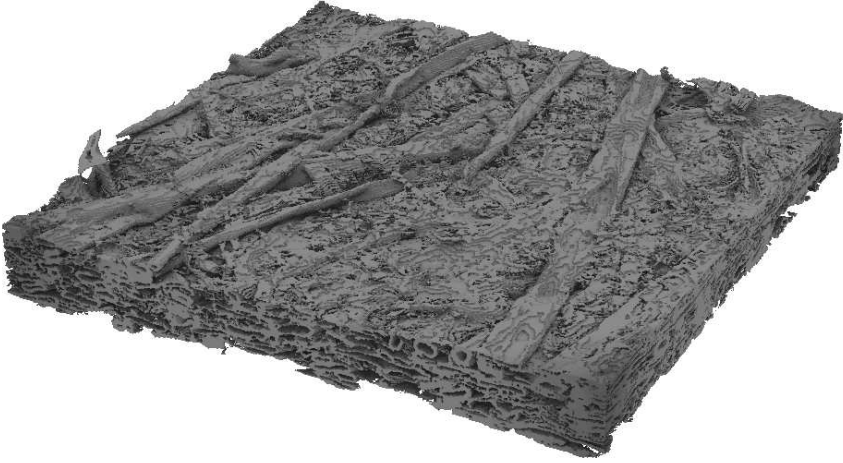


(a)

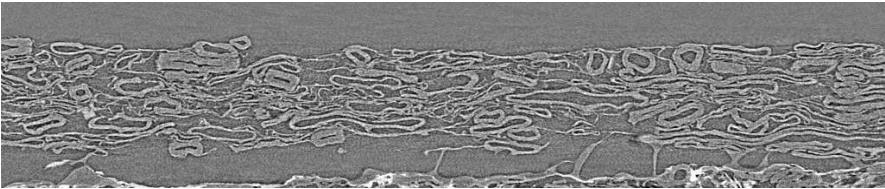


(b)

Figure 11: Five layered cardboard. (a) Surface rendering of the fibre network. (b) Original X-ray microtomography data showing the front slice of the volume.



(a)

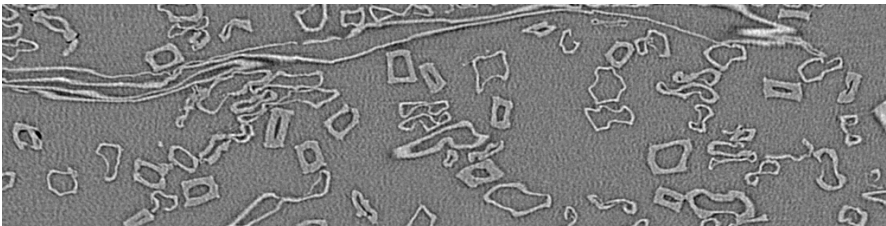


(b)

Figure 12: Newsprint. (a) Surface rendering of the fibre network. (b) Original X-ray microtomography data showing the front slice of the volume.

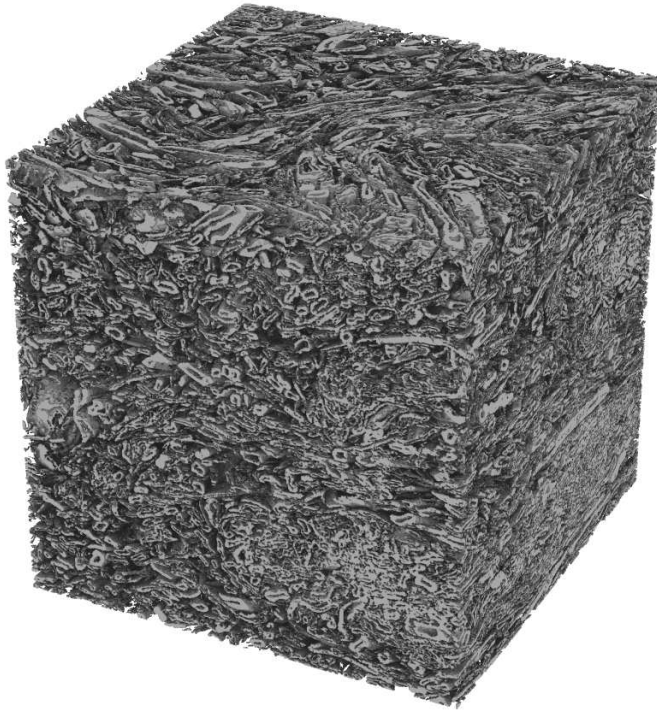


(a)

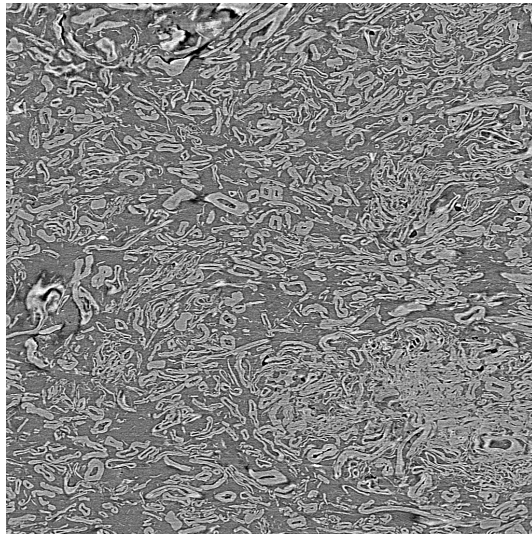


(b)

Figure 13: Wood fibre composite material. (a) Surface rendering of the fibres in the material. The matrix is made transparent. (b) Original X-ray microtomography data showing the front slice of the volume.

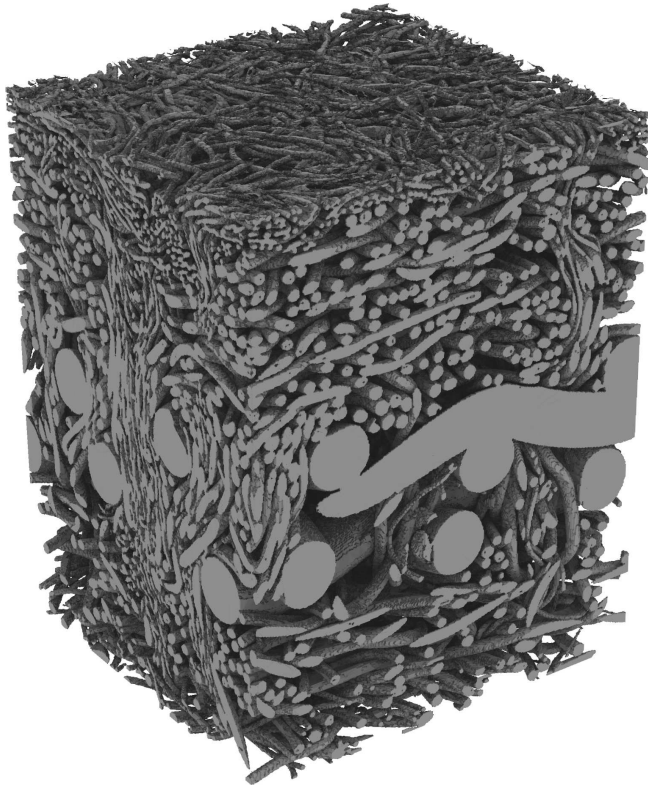


(a)

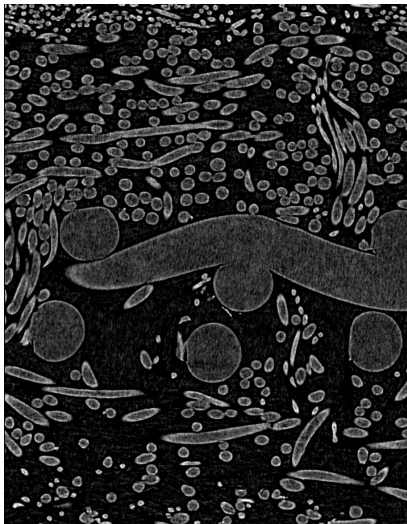


(b)

Figure 14: Wood fibre composite material. (a) Surface rendering of the fibres in the material. The matrix is made transparent. (b) Original X-ray microtomography data showing the front slice of the volume.



(a)



(b)

Figure 15: Press felt. (a) Surface rendering of the fibres in the material. (b) Original X-ray microtomography data showing the front slice of the volume.

4 Preprocessing

The first step in many image analysis methods is noise and artifact reduction. Images always contain noise and often other artifacts as well. These are caused by imperfections in the measurement equipment. There are many ways to suppress noise and artifacts, both during the image acquisition and afterwards in the digital images. It is always best to reduce noise and artifacts as early in the process as possible.

In this thesis, most image analysis methods are exemplified using X-ray microtomography images. Both noise and artifacts are present in the reconstructed images and need to be reduced before further analysis of the images. Noise and artifacts are more common in synchrotron X-ray microtomography images than in images acquired by commercial tomography systems. This may be due to the fact that most synchrotron facilities conduct research on the beamline itself whereas commercial systems need to be competitive on the market and hence more time is spent on processing the acquired data. One specific type of artifact is ring artifacts, which is a problem in most tomography systems. Methods suitable for reducing both ring artifacts and noise are presented in this chapter.

4.1 Ring artifact reduction

Ring artifacts occur in reconstructed images from X-ray microtomography as full or partial circles centred on the rotation axis of the scanning system. The ring artifacts are additively superimposed on the images as constant higher or lower pixel values on equal radius from the centre of rotation. Figure 16(a) shows an image with a strong ring artifact in the left half of the image. The main cause for the ring artifacts is that pixel values in the collected radiographs (projections) have an offset and do not correspond directly to the attenuation of the incoming X-ray beam. In the reconstruction of the volume images the offset of a single pixel which is not calibrated traces a circle or a half circle in the volume in the plane perpendicular to the rotation axis. If the offset is large there is no information about the attenuation of the beam. This results in saturated ring artifacts in the reconstructed images.

Offset values in the radiographs and the resulting ring artifacts, can occur due to variations in the incoming beam such as intensity variations or imperfections (Antoine et al., 2002), differences in detector element gain (Vidal et al., 2005), or variations in the beam together with effects of the point spread function of the detector elements (Cloetens, 1999). Some ring artifacts can be reduced by calibrating the tomography system using for example flat-field correction (Cloetens, 1999). An image of only the detector and the beam, called a bright image, and an image without the beam, called a dark image, are used to correct the recorded radiographs. Some tomography systems use translations of the detector to reduce ring artifacts that are due to defective detector elements (Jenneson et al., 2003). Filtering methods applied to the radiographs have also been used to reduce ring artifacts before the reconstruction, see for example Raven (1998); Tang et al. (2001).

It is always better to reduce artifacts before the images are reconstructed. However, in some cases there are still artifacts in the reconstructed images that need to be removed before further processing. One method for reducing ring artifacts in the reconstructed images was presented by Sijbers and Postnov (2004). In their method the reconstructed images are transformed to polar coordinates, where the ring artifacts occur as line artifacts. The artifacts are reduced in polar coordinates and the images are transformed back to Cartesian coordinates. It is assumed that the rings are full circles and no distinction is made between pixels with and without artifacts.

Paper I presents a new method for reducing ring artifacts in reconstructed high resolution X-ray microtomography images. It is a 2D method which is applied to slices perpendicular to the rotation axis, since the artifacts occur as rings in these slices. The ring artifacts are best reduced before noise reduction is applied to the images, since the properties of the ring artifacts are distorted by the noise reduction.

The presented method is based on local orientation estimation of the image structures (Granlund and Knutsson, 1995). First, a local structure tensor is estimated in each pixel neighbourhood using four quadrature filters. The structure tensor can be represented by a 2×2 symmetric matrix in 2D. The eigenvectors and eigenvalues of each tensor contain information about the local orientation and the tensor anisotropy. The local orientation is obtained from the eigenvector that corresponds to the largest eigenvalue. The vector is oriented parallel to the largest signal variation. Figure 17(a) shows the estimated local orientation for the image in Figure 16(a) using varying colours for the different orientations. Each orientation estimate can be associated with a corresponding certainty value, c_1 , calculated from the eigenvalues of the tensor as

$$c_1 = \frac{\lambda_1 - \lambda_2}{\lambda_1} \quad (2)$$

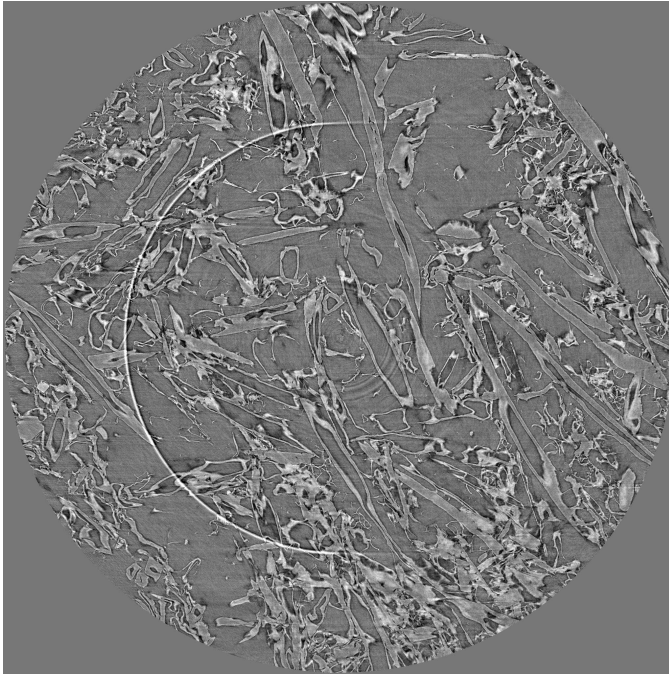
where λ_1 and λ_2 are the largest and second largest eigenvalues. In neighbourhoods where c_1 is large, λ_1 is large relative to λ_2 , which corresponds to signal variation in one dominant orientation and an anisotropic tensor.

Local orientations in the image that correspond to circular patterns around the rotation axis are identified. The scalar product between the normalised first eigenvector of each tensor, $\hat{\mathbf{e}}_1$, and a normalised vector from the centre of rotation, $\hat{\mathbf{r}}$, is used as

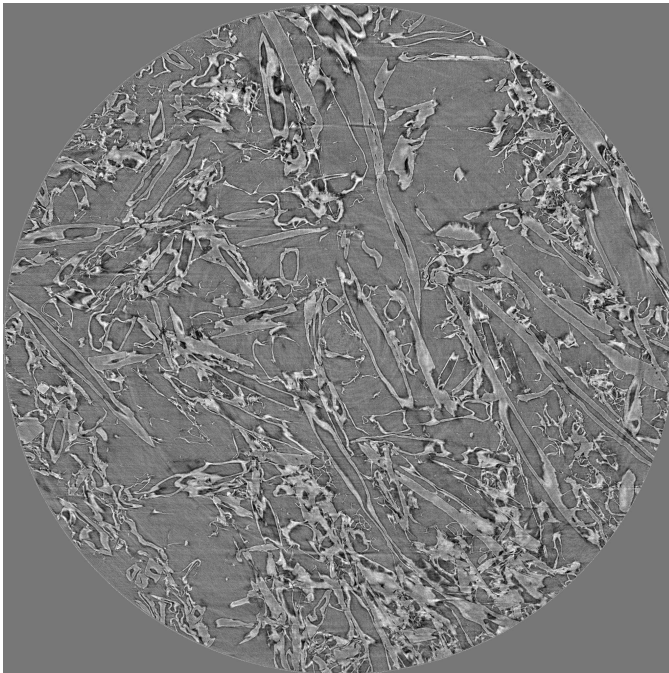
$$c_r = |\hat{\mathbf{r}} \cdot \hat{\mathbf{e}}_1|^n \quad (3)$$

where the absolute value of the scalar product is sharpened by an exponent, n , since the cosine function is too wide in most cases. The c_r value is pixel-wise scaled by the c_1 value and the image is resampled to polar coordinates, where it is smoothed along the radii to create a certainty image for the artifacts. Figure 17(b) shows the certainty image for the original image in Figure 16(a). The original image is also resampled to polar coordinates and used together with the certainty image to calculate a correction image, using normalised convolution by Knutsson and Westin (1993). Normalised convolution is a method for filtering images with uncertain measurements by associating each pixel with a certainty value. It is calculated as

$$I_e = \frac{a * cI}{a * c} \quad (4)$$

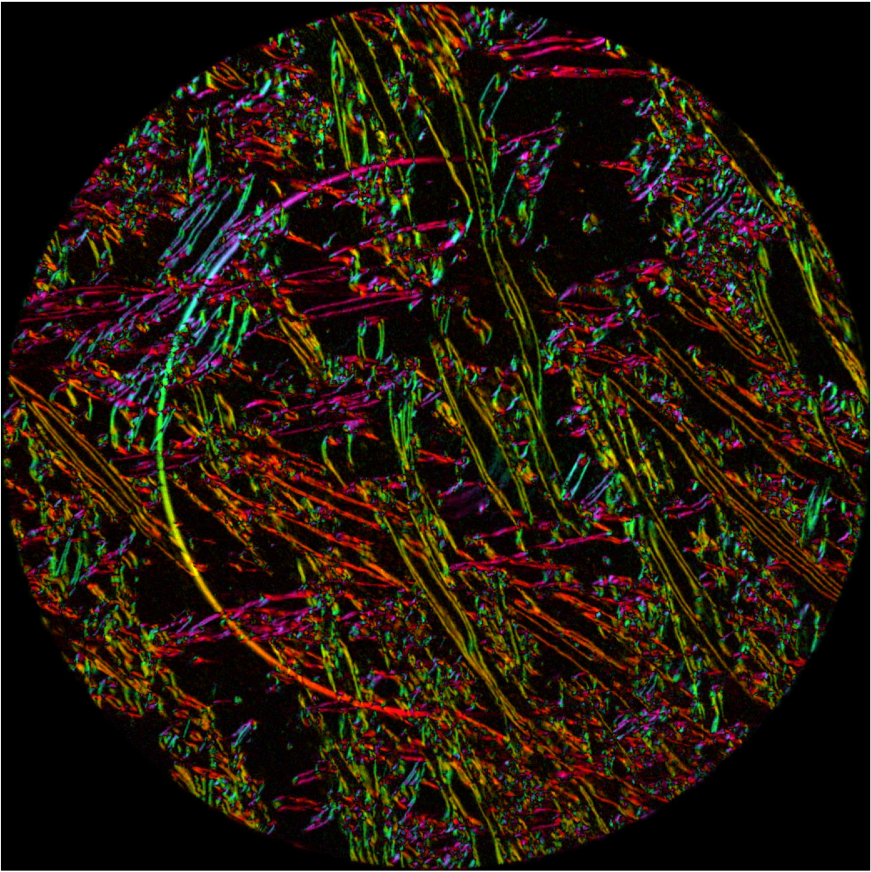


(a)

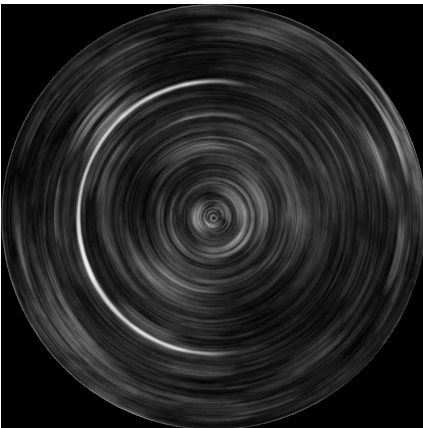


(b)

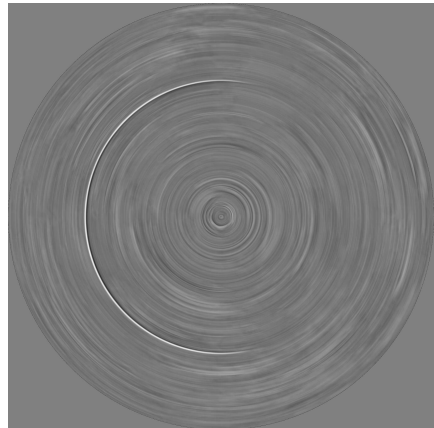
Figure 16: Ring artifact reduction in an X-ray microtomography image. (a) Original image. (b) Corrected image.



(a)



(b)



(c)

Figure 17: Intermediate steps of the ring artifact reduction method. (a) Estimated orientations in the image illustrated using varying colours. (b) Certainty image. (c) Correction image.

where I is the input image, c is the certainty image, and a is called an applicability function. Normalised convolution is applied to only take pixels that are affected by the artifacts in account in the averaging. In this case the applicability function is a one pixel wide kernel in the radial direction and has a fixed length in the angular direction, except close to the origin where shorter filters are used. The correction image is resampled to Cartesian coordinates. See Figure 17(c) for an example of a correction image. The correction image is adjusted to have values that vary around zero by subtracting a constant, which can usually be set to the centre value of the dynamic range of the image. The artifacts in the input image are reduced by subtracting the correction image in all pixels proportionally to the values in the certainty image. Figure 16(b) shows the corrected image.

The images used for evaluation of the method were 2D images from a set of X-ray microtomography images of paper imaged at beamline ID19 at ESRF. Both images with and without artifacts were present in the evaluation set. Figure 18 shows results for non-saturated ring artifacts. As can be seen in the figures, the method can reduce both full and partial ring artifacts. In Figure 19 the result for a partly saturated ring artifact is shown. It is not possible to recover all pixel values for saturated artifacts, since the information about the underlying densities is lost.

One of the main features of the presented method is that the original image resolution is not altered by resampling the image, since the image is corrected directly in Cartesian coordinates. Another of the main features is that the artifacts are estimated and corrected locally for reduction of both full and partial rings. In addition, only the pixels estimated to contain artifacts are changed in the correction step.

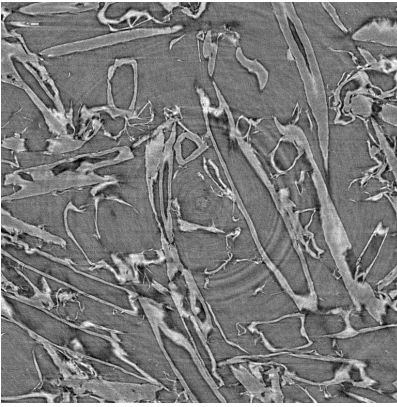
In future work it may be interesting to investigate the applicability of the method to other types of tomography images. Another topic for future work is possible correction methods of the completely saturated pixel values using 3D information.

The ring artifact reduction was applied to all volume images from the ESRF ID19 before further processing of the images using the methods presented in this thesis. The ring artifacts in the volume images from PSI Tomcat were reduced before the reconstruction of the images using a method applied directly on the radiographs.

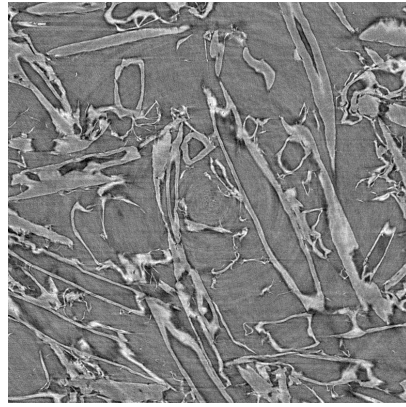
4.2 Noise reduction

Noise is undesired distortion of a measurement. All measured images contain noise, and therefore noise reduction is a common preprocessing step in automated image analysis.

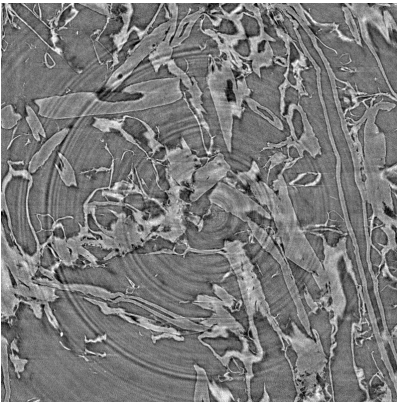
Noise in X-ray microtomography images can be reduced in many ways. Noise can be reduced in the imaging, by selecting a longer integration time when scanning the sample. However, the scanning time is limited and some noise in the images must be accepted. Noise can also be reduced after the reconstruction of the images. One of the simplest approaches to reduce noise is Gaussian filtering of the image using an isotropic filter mask. The Gaussian filter reduces high frequency content in the image. Thereby noise in the image is reduced. However, edges are blurred since



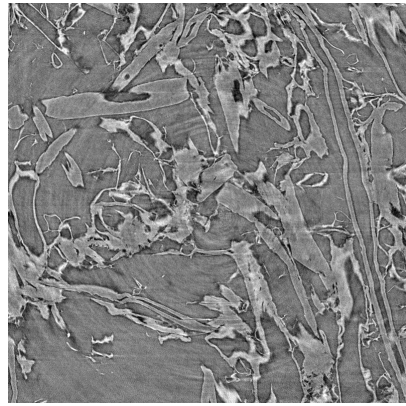
(a)



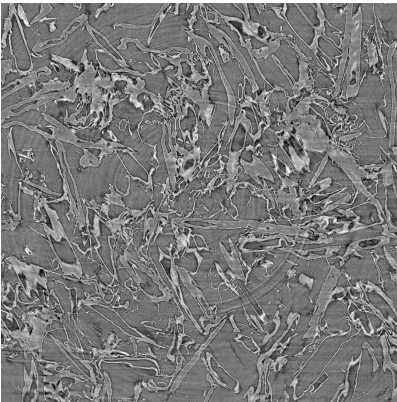
(b)



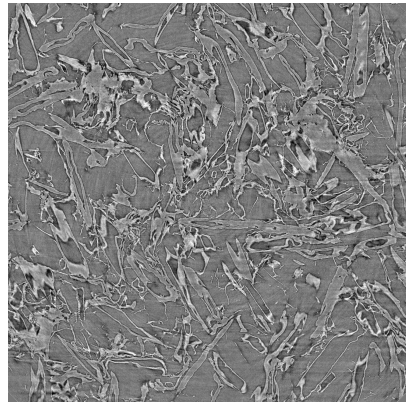
(c)



(d)

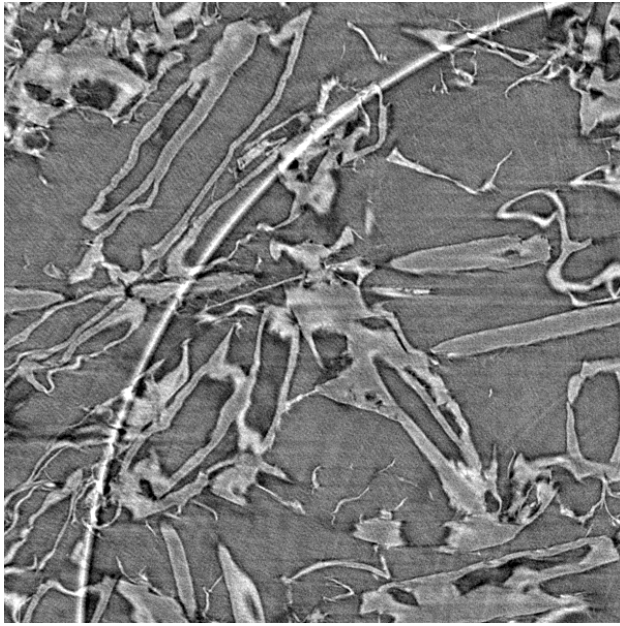


(e)

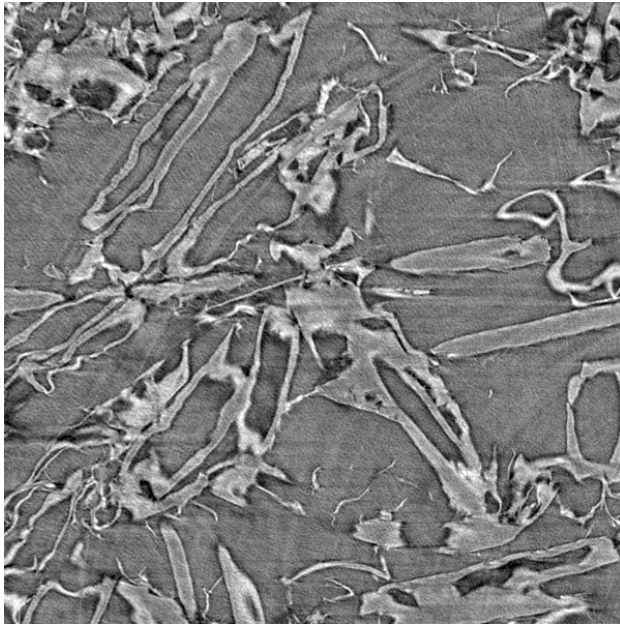


(f)

Figure 18: (Left) Reconstructed X-ray microtomography images with ring artifacts. Note that these images are cropped. (Right) After ring artifact reduction using the presented method.



(a)



(b)

Figure 19: (a) A partly saturated ring artifact. (b) Corrected image. Note that the saturation of some pixel values limits the reduction of the artifact since the pixels do not contain information about the underlying densities.

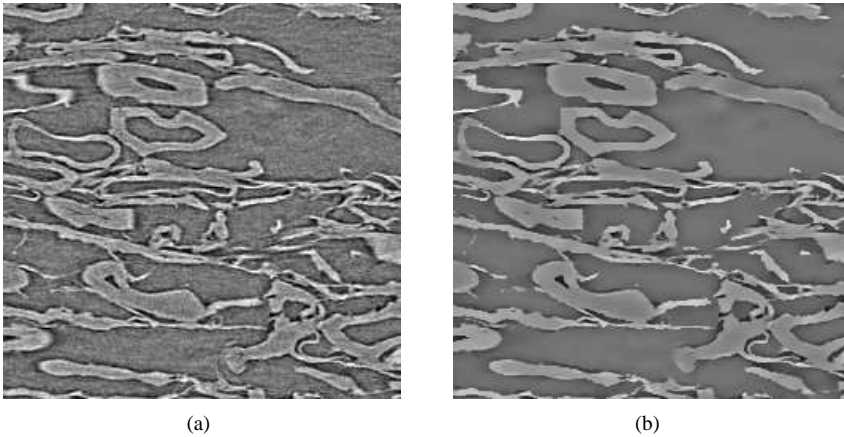


Figure 20: (a) Original image. (b) Noise reduction using 3D SUSAN filtering.

they contain high frequencies. Other approaches, which reduce noise but preserve edges, are preferable. Non-linear smoothing techniques, where a filter kernel is adapted to the image structures in a local neighbourhood, can be used.

Some of the most common methods for non-linear noise reduction are anisotropic diffusion (Perona and Malik, 1990), bilateral filtering (Tomasi and Manduchi, 1998), SUSAN filtering (Smith and Brady, 1997), and adaptive filtering (Granlund and Knutsson, 1995). 3D versions of these methods can be applied to reduce noise in X-ray microtomography images. 3D filtering methods produce better results than 2D filtering for volume images, since the available information about edges and image structures is better used in the 3D filtering and more data points are used when averaging. The suitability of the 3D versions of all of the mentioned filtering methods has been investigated for X-ray microtomography images of paper by Fransson (2007), who concluded that all the tested methods can be tuned to give satisfactory results for the volume images.

In Paper III noise is reduced in the volume images using 3D SUSAN filtering prior to binarisation (Section 5.1.1). In SUSAN filtering two Gaussian filter kernels, a spatial filter and a range filter, are combined to select weights for the voxels that should be used in the averaging. The spatial filter is based on spatial distance and the range filter is based on difference in image intensity. This is similar to bilateral filtering with the difference that the centre element is not used in the filtering, which reduces impulse noise. An example of 3D SUSAN filtering applied to an X-ray microtomography image is shown in Figure 20.

The noise level in the X-ray microtomography images depends on the beam quality and the imaged material. The parameters for noise reduction often have to be adjusted using manual inspection of each volume, which makes noise reduction difficult to automate in a robust way.

5 Pore structure characterisation

This chapter presents new methods for pore structure characterisation of paper and press felts. Section 5.1 describes methods for characterisation of the 3D pore structure in paper using volume images. Section 5.2 presents a method for estimation of the interface pore volume between paper and press felt under load using confocal microscopy images of press felts.

5.1 3D Pore structure characterisation of paper

The pore structure in paper and other porous materials governs important material properties such as print properties and transport properties for fluids. These are determined both by the surface pore structure and the pore network. The properties of the pore structure can be determined by characterising the material microstructure.

The 3D pore structure of paper has predominantly been studied using X-ray microtomography images. Different approaches have been used depending on the desired measurements. Methods for characterisation of the pore structure of paper using X-ray microtomography images have been proposed for example in Ramaswamy et al. (2001, 2004); Huang et al. (2002); Holmstad et al. (2005, 2006); Goel et al. (2006).

Paper II and Paper III present new 3D image analysis methods for pore structure characterisation of paper, with new pore structure representations and corresponding measurements. The methods are intended for large volume images, such as data sets from X-ray microtomography. The methods are outlined in the following sections.

5.1.1 Binarisation

The pore structure is characterised by analysing the void space in the material. The voxels in the void space in X-ray microtomography images have even intensity and the variation of the values does not add information about the structure or shape. See for example the X-ray microtomography image in Figure 7. Due to this fact, we analyse the pore structure using binary images.

Binarisation is classification of the elements in an image into object and background (fibre and void). Sometimes binarisation is also referred to as segmentation. Ideally, a threshold is applied to an image where the histogram shows a clear separation between object and background. However, in practice this is often difficult due to lack of separation between object and background with respect to pixel values, low contrast, or noise in the images. Binarisation is an important step, since all measurements on the binary image depend on the segmentation into fibre and void.

Different methods have been suggested for binarising X-ray microtomography images of paper and other wood fibre-based materials. Antoine et al. (2002) presented the first method for binarisation of phase contrast images. A more advanced method based on graph-cuts was proposed by Malmberg (2008). In Rolland du Roscoat et al. (2005b) absorption mode images were binarised using seeded region growing.

In many of the X-ray microtomography images that are used to exemplify the methods presented in this thesis there is only a small difference between the values of the background and object voxels and the images contain noise. For an example, see the histograms of the four X-ray microtomography images in Figure 10. Noise can be reduced using the methods discussed in Section 4.2.

In Paper III we propose SUSAN smoothing (Smith and Brady, 1997) and hysteresis thresholding (Canny, 1986) for binarisation of absorption X-ray microtomography images. In hysteresis thresholding one high and one low threshold are used. The voxels classified as object in the higher thresholded image are used as seed points, from which region growing is allowed where there are connected voxels classified as object in the lower thresholded image. This produces a result where all final object voxels are connected to voxels from the higher thresholded image. After binarisation the object regions are labelled. All regions, except the largest, are considered as background, since the fibre network in paper is assumed to be one connected component.

5.1.2 *Finding the paper surface*

The surface structure of paper is porous. The surface pores are important, for example, for printing and optic properties. However, the paper surface is not easily defined. One method for estimating the paper surface, which takes the surface pores into account, is the rolling ball method that was originally introduced by Sternberg (1983). It was suggested for estimation of paper surfaces in Aronsson (2002b); Svensson and Aronsson (2003).

In the rolling ball method, the surface of the paper is outlined by simulating a ball rolling over the material. The radius of the ball determines the smoothness of the estimated surface. An infinite radius generates planar surfaces. A suitable radius must be selected depending on the intended application and the desired measurement. Figure 21 shows an example where the pore space of paper has been defined using the rolling ball method to estimate the top and bottom surface of a cardboard sample. The fibres are shown in grey, the pore structure in black and the outside void space in white.

The rolling ball method was applied in Paper II and Paper III to estimate the paper surface and in Paper IV to estimate the indentation of the paper surface into surface pores of press felt. The rolling ball can be efficiently implemented using distance transforms, as proposed in Svensson and Aronsson (2003).

5.1.3 *Segmentation of individual pores*

Paper II presents a new pore space representation, the individual pore based representation, where the pore space in volume images of paper is divided into separate regions called individual pores. Characterisation of the pore structure can be performed by measuring individual pores and their interrelations.

The presented method takes a binary volume image of the identified pore space as input. A distance transform is applied to the image. The distance transform calculates the shortest distance from the background to each object voxel. We apply

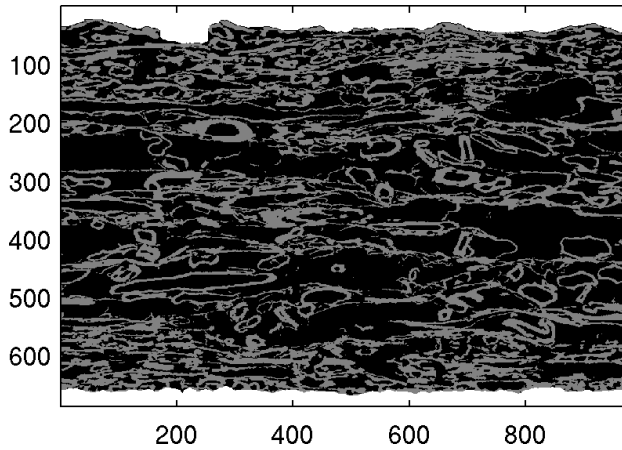
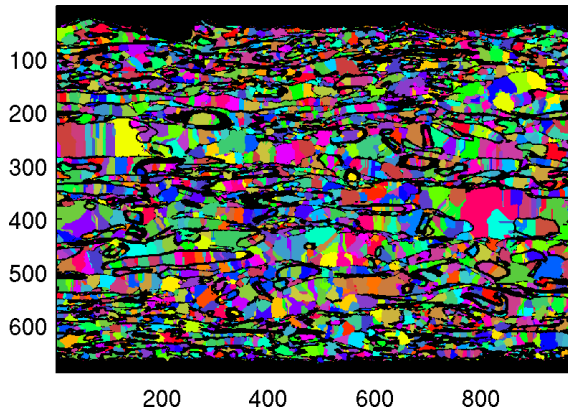


Figure 21: Identified pore space, where the rolling ball method has been used to outline the surface of a binary fibre network. The fibre network is shown in grey, the identified pore space in black, and the estimated surface is the interface between the white (outside) and the black or grey voxels (inside).

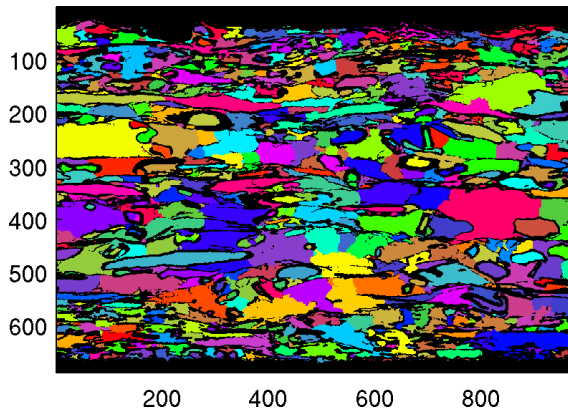
a weighted distance transform, where the distance to a face neighbour is weighted 3, an edge neighbour 4, and a vertex neighbour 5, as proposed by Borgefors (1996). For non-cubic voxels, which are common in images from many imaging devices, the method proposed by Sintorn and Borgefors (2004) is used. In Paper II this was applied to the volume image reconstructed by Aronsson et al. (2002).

The watershed algorithm (Beucher and Lantuéjoul, 1979; Vincent and Soille, 1991) is a general segmentation method that divides an image into separate regions based on, for example, image intensity, distance information, or gradient magnitude. Each local maximum is the seed of one region and a regionalisation of the image is created using region growing from the seeds. In Paper II the watershed algorithm is applied to the distance transform of the pore space. Each local maximum in the distance transform generates one region. This usually gives an over-segmented image. Figure 22(a) shows an example of the watershed segmentation applied to the distance transform of the pore space.

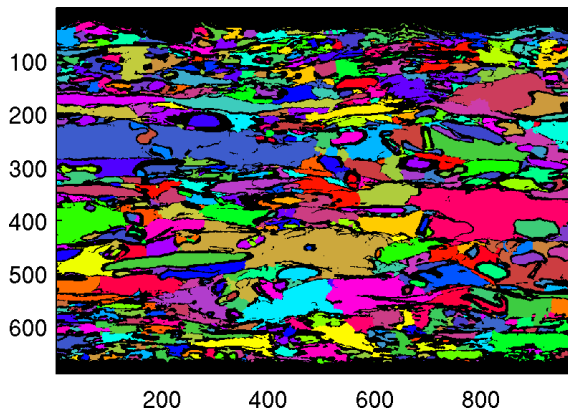
Pairs of regions from the watershed segmentation can be merged to reduce the over-segmentation and obtain a final regionalisation of the image. In Paper II, the regions are merged using two criteria. The distance maximum in each region and the distance maximum on the interface between the regions are used in the merge criteria. The first criterion merges regions where the smaller of the two region maxima is only slightly larger than the maximum on the connecting interface. This merges regions where only a small contraction of the structure, or noise, creates two separate maxima in the distance transform. Figure 22(b) shows the regionalisation after the first merge of the regions in (a). The second criterion merges regions where the maximum on the connecting interface is larger than a threshold value. This gives regions, individual pores, in the final segmentation which are separated by narrowings, throats, with a maximal throat size. Figure 22(c) shows the final segmentation



(a)



(b)



(c)

Figure 22: Segmentation of individual pores in an X-ray microtomography image of a cardboard sample. (a) Watershed segmentation of the identified pore space in Figure 21. (b) Regionalisation after the first merge. (c) Final segmentation of the individual pores.

into individual pores using the presented method. Figure 23(a) shows a volume rendering of the segmented pore space in a part of the sample.

The segmentation of individual pores does not provide a segmentation of specific entities in the pore structure, but provides statistics about the pore structure of a sample. Different parameter setups result in different pore space divisions. The variation between different materials or samples can be studied by using the same parameters for all images.

In Chinga et al. (2008) the segmentation of individual pores was applied in a study of print-through in newsprint samples and in Turpeinen et al. (2008) it was used to estimate the pore size distribution by simulating mercury intrusion porosimetry.

5.1.4 Individual pore based skeleton

In Paper III we introduce a new pore space representation, the individual pore based skeleton, which is suitable to characterise the pore network. Measurements such as permeability or flow through the material can be studied as a function of path length.

The individual pore based skeleton is based on the individual pore representation of the pore space described above. Each individual pore is represented by the corresponding maximum in the distance transform. Each pair of pores that share an interface is connected by a path passing through the maximum on the connecting interface. The path is obtained by computing the constrained distance transform (Piper and Granum, 1987) from the maximum on the connecting interface onto the two pores. The path is found by path growing from the two distance maxima in the pores in the direction of the steepest gradient. This results in a simple curve representation of the pore space. In contrast to the more complex distance based skeleton (Lindquist et al., 1996; Lindquist and Venkatarangan, 1999; Baldwin et al., 1996) this new pore space representation contains fewer curves and no surfaces. Because of the simpler structure, it is more suited for measurements on the pore structure. Figure 23(b) shows a volume rendering of the individual pore based skeleton obtained using the individual pore segmentation in (a).

5.1.5 Measurements on the pore structure

Characterisation of the pore structure in paper can be performed using different representations of the pore space. In Paper III measurements for the binary pore space representation, the individual pore representation, and the individual pore based skeleton are presented. The binary pore space representation is the simplest representation of the pore space. Figure 21 shows an example of the binary pore space after the paper surfaces have been estimated using the rolling ball method.

Measurements such as porosity and surface area of the pore network can be measured on the binary pore space representation. For the individual pores more measurements are available, such as volume, surface area, interface area, connectivity, orientation, and anisotropy. Also distributions of the pores are available, such as pore frequency and pore size distributions. The measurements can be averaged over

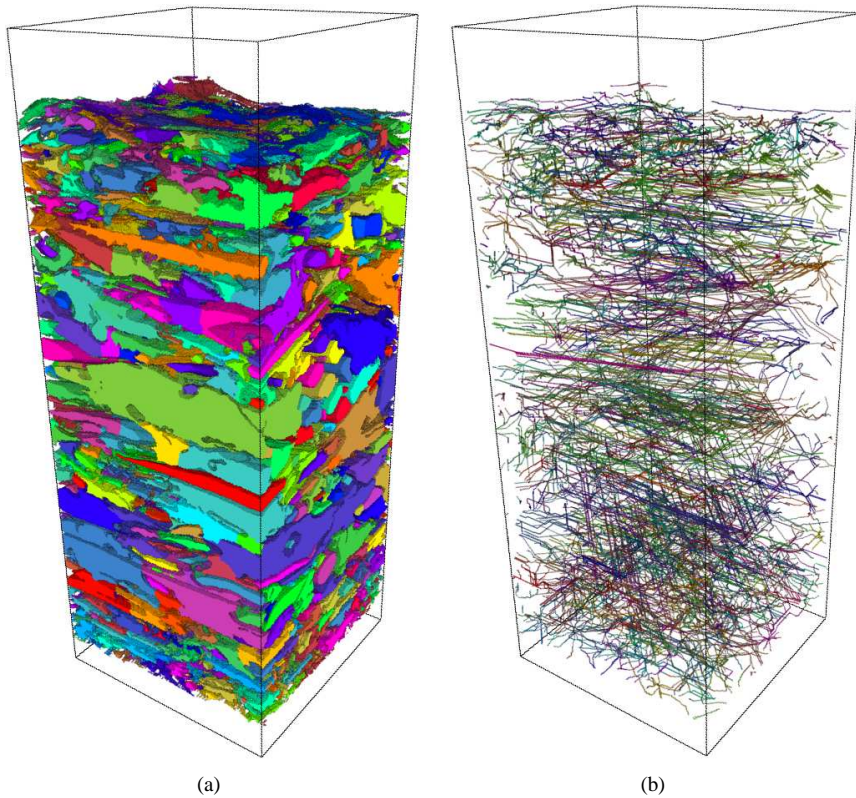


Figure 23: Volume renderings of the presented pore space representations for a part of a cardboard sample. (a) Individual pore based representation. (b) Individual pore based skeleton.

different layers of the sheet or other divisions of the sample. One particularly interesting measurement is the orientation and anisotropy of the individual pores. This can be measured using Principal Component Analysis (PCA) of each individual pore, as described in Paper III. The pore orientation gives an insight to the physical sample orientation as the fibres tend to be oriented in the machine direction. The anisotropy provides an estimate of the elongation of the pores. For the individual pore based skeleton the same measurements as for the distance based skeleton can be obtained. For example, different pore size distributions based on the values in the skeletal voxels can be measured. In Paper III we compare the results obtained using the different representation and show that the new representation can be used equivalently to the more common distance based skeleton. We also show that the new representation is suited to estimate tortuosity.

The presented pore space representations and the corresponding pore measurements are general and may also be used to characterise the pore structure in other porous materials. Evaluation of the applicability of the methods to other materials is left for future work.

5.2 Estimation of the pore volume between paper and press felt

In addition to the pores in paper, the pore structure is also important in the design of other porous materials. The pore structure of press felt determines its water holding capacity and subsequently the efficiency of the dewatering. Different surface characteristics are needed for different dewatering situations. Better understanding of how the pore structure affects the dewatering can be gained by characterisation of the pore structure.

Paper IV presents a new image analysis method for estimation of the pore volume at the interface between paper web and press felt. The method is intended for application to volume images of press felts under load. The volume images are acquired in a CLSM using a compression device, where a glass plate is pressed against the sample using different loads. Figure 24 shows a slice of an example volume image parallel to the surface of the sample and two perpendicular slices. It is clearly visible that the attenuation of the fluorescent signal in the fibres is large. Thus, only the topography of the sample can be obtained in the volume image using this technique.

A topography map is calculated from each volume image. The surface of the fibres is identified as voxels with high intensity. For each line of voxels in the depth direction, the position of the surface is calculated as the centre of mass for voxels above a noise threshold with the voxel intensities as weights. For lines where no voxels have values above the noise threshold, the background depth is set. The zero level of the topography map is adjusted by identifying the first slice with fibres in the input volume. As the felt is compressed against the glass, the first slice with fibres can be easily detected using a threshold. Figure 25(b) shows the topography map for the volume in (a).

Two types of artifacts are common in the volume images. These affect the estimated topography map, which needs to be corrected. One problem is a self shadowing effect on the fibre edges. This causes low intensities in the volume image even if a fibre is crossing underneath. Another problem is stains on the fibre surface that also cause low intensities in the input volume. Figure 25(a) shows a sum projection of a volume image. The two types of artifacts are visible in the sum projection as pixels with low intensity. The artifacts can be efficiently removed from the topography maps using normalised convolution presented by Knutsson and Westin (1993), where a certainty map with a value for each depth measurement is used together with a small Gaussian filter as the applicability function. See also Section 4.1. The applicability function should be smaller than the fibre radius and large enough to smooth stains and dark areas between the fibres. The certainty map contains ones for all values in the topography map that were calculated using at least one voxel. Otherwise the map is set to zero. Figure 25(c) shows the certainty map. Here, the map is binary, but all values in the range between zero and one may be used if needed. The normalised convolution also removes some imaging noise by smoothing. Figure 25(d) shows the topography map after it has been corrected using normalised convolution.

To estimate the pore volume at the interface between the felt and the fibre web the indentation of the fibre web also needs to be estimated. The indentation is ob-

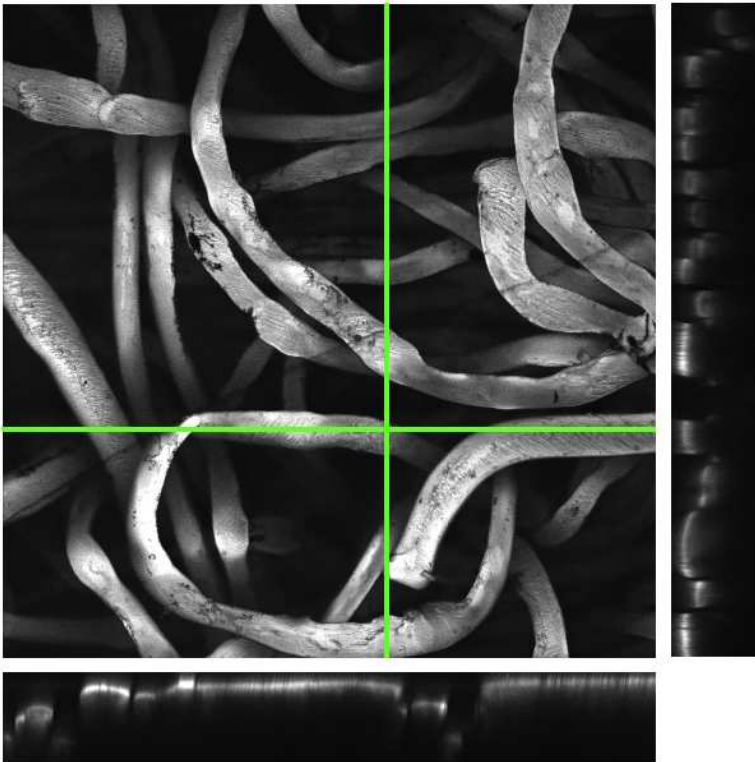


Figure 24: Press felt under a load of 2 MPa imaged using CLSM. The top left image shows a slice of the volume image parallel to the surface of the sample. The other two images show perpendicular slices at the positions marked by the lines.

tained by applying the rolling ball method (Section 5.1.2) to the topography map after it is converted to a binary volume. The weights of the distance transform used in the rolling ball method are optimised for the non-cubic voxels in the CLSM images (Sintorn and Borgefors, 2004). The radius of the rolling ball is set to the radius of curvature of the indented fibre web.

The pore volume at the interface is obtained by subtracting the indentation of the fibre web from the topography map of the felt. Figure 26 shows a surface rendering of the spatial distribution of the estimated interface pore volume. The presented method was used in a case study of four press felts in Paper IV.

More detailed measurements of the interface pore volume can be obtained using X-ray microtomography images of press felts (Thibault et al., 2002). Volume images of felt and web together under load can be used to estimate the true interface pores. The methods for pore structure characterisation of paper in Section 5.1 are expected to be directly applicable to press felts in volume images or images of the interface between felt and web under load. This may be interesting to study in future work.

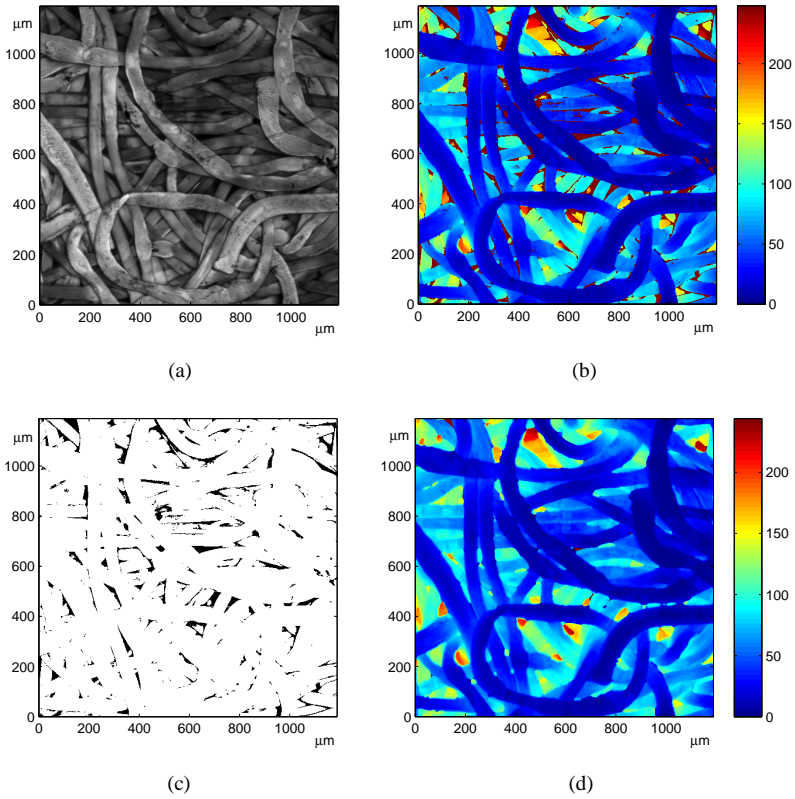


Figure 25: Press felt under a load of 2 MPa imaged using CLSM. (a) Sum projection of the entire volume in the Z-direction. (b) Topography map of the estimated surface without correction of artifacts. (c) Certainty map. (d) Topography map of the estimated surface corrected using normalised convolution.

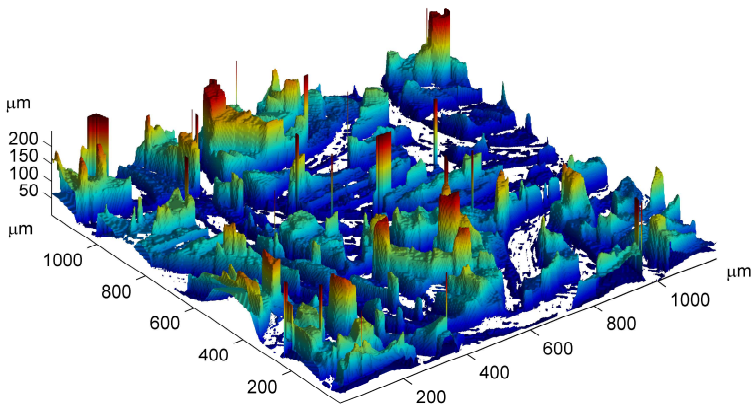


Figure 26: Surface rendering of the spatial distribution of the estimated interface pore volume for a load of 2 MPa.

6 Fibre segmentation

In order to measure properties such as length, fibre wall thickness, slenderness ratio, curl, twist, degree of collapse, and relative bonded area of individual wood fibres each fibre must be segmented individually. If all fibres are individually labelled in a volume image, many measurements on the fibres or the fibre network can be obtained. In addition, it is possible to use the measurements to model fibre network properties such as strength, optical properties, and transport properties. This, in turn, makes it possible to engineer paper sheets and fibre reinforced composite materials with improved properties. A complete segmentation of individual fibres in volume images is a main goal in the development of new methods for analysis of fibre-based materials. However, there are no fully automatic methods available for segmentation and labelling of individual fibres. Segmentation is difficult, since all fibres are connected and the network can be very compact. See examples of different fibre network structures in Chapter 3.

Some efforts have been made to solve the problem of automatic segmentation of individual fibres. Aronsson and Borgfors (2001) presented a method for automatic detection of ring shaped objects. The method was also adapted to non-cubic voxels in Aronsson and Sintorn (2002). The results from individual slices were combined to parts of individual fibres, see Aronsson (2002b). Measurements for individual fibres were presented in Aronsson (2002a); Svensson and Aronsson (2001, 2003). The volume image that was used in their studies was the sample described in Aronsson et al. (2002). A similar approach to that of Aronsson (2002b) was first proposed by Holen and Hagen (2004) and then refined by Bache-Wiig and Henden (2005). X-ray microtomography images were used in both studies. A method based on morphological lumen segmentation and seeded region growing was proposed by Walther et al. (2006). A method using Maximally Stable Extremal Regions was proposed by Donoser and Bischof (2006) for volume images from light microscopy (Wiltsche, 2005). Recently, Donoser et al. (2008) also proposed a method using particle filters for tracking fibres.

All previously proposed methods except for Walther et al. (2006) use slice based approaches for segmenting the individual fibres in image cross sections. See Figure 27(a) for an example of an image cross section. The variation of fibre shapes and sizes is large in the image cross sections and many of the previously proposed methods have problems with cracked or collapsed fibres. These problems must be handled explicitly in each method. In Walther et al. (2006) cracked and collapsed fibres also affect the applied lumen segmentation.

Paper V introduces a new approach to segmentation of individual wood fibres, where 3D information in a neighbourhood around each point is used to track tubular structures through the volume. The idea in Paper V is to use local sum projections of the volume around each fibre and identify the fibre wall as two lines with higher intensity in each sum projection. This can be used to track individual fibres in volume images. Problems with cracked or collapsed fibres are then handled implicitly. Even almost completely collapsed fibres can be tracked using the new approach. The variation between different fibres is also smaller in the sum projections than in

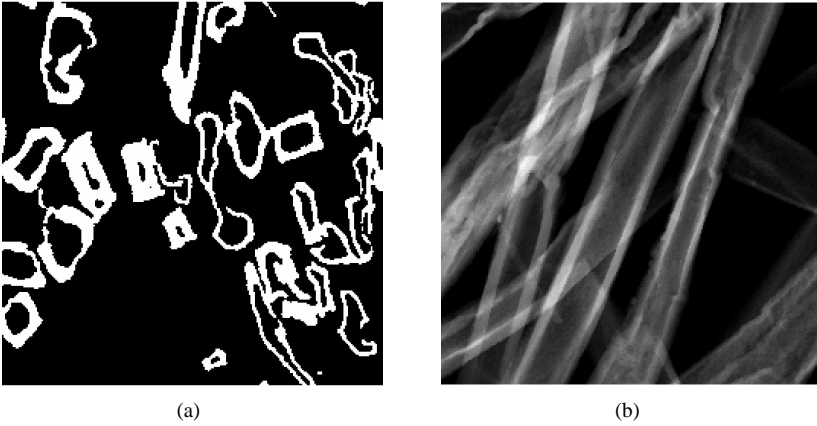


Figure 27: (a) Image cross section from a binary volume image. (b) Sum projection of a part of the same volume image. (Image from Paper V.)

the cross sections. Figure 27(b) shows an example of a sum projection. Note that this is the projection of a larger part of the volume than the local projections that are used in the method.

The tracking starts in manually placed seed points. A seed consists of a point, \mathbf{m}_0 , inside the fibre lumen and a vector, \mathbf{v}_0 , which is oriented approximately in the local fibre direction. A fibre is tracked using a local coordinate system that follows the local fibre direction \mathbf{v} . The origin of the coordinate system is placed at the current tracking position \mathbf{m} . The coordinate system that is used in the fibre tracking is illustrated in Figure 28(a), where \mathbf{x} , \mathbf{y} , and \mathbf{z} defines the image coordinate system and \mathbf{v} , \mathbf{x}' , and \mathbf{z}' defines the local coordinate system used for calculating sum projections of the volume around the fibre. The local coordinate system is derived from the global coordinate system as $\mathbf{x}' = \mathbf{z} \times \mathbf{v}$ and $\mathbf{z}' = \mathbf{v} \times \mathbf{x}'$.

First N evenly distributed local sum projections of the volume are calculated perpendicular to \mathbf{v} . Four sum projections have shown to be suitable for wood fibres. Projections are calculated in the \mathbf{x}' and \mathbf{z}' directions. Then, the local coordinate system is rotated $\pi/4$ radians around the \mathbf{v} axis and two more projections are calculated along the same coordinate axes. Figure 29(a) and (f) show the slice perpendicular to \mathbf{v} at the current tracking position \mathbf{m} for two examples. Figure 29(b–c) and (g–h) show the two sum projected images in the two directions parallel to \mathbf{v} .

The size of the projected volume in the \mathbf{x}' and \mathbf{z}' directions is either determined by information from previous tracking steps or from the initialisation values at the first step. In the projection direction only the interior of the fibre is used to calculate the sum projection. In the other direction perpendicular to \mathbf{v} the volume is padded to include a part outside the fibre wall in the sum projection. Position estimates of the fibre wall and fibre cross sectional dimensions from previous tracking steps are used to make the volume size adaptive to changes of the fibre dimension. A fixed volume size is used in the \mathbf{v} direction. Additional projections can be used to avoid problems with occlusion for almost collapsed fibres.

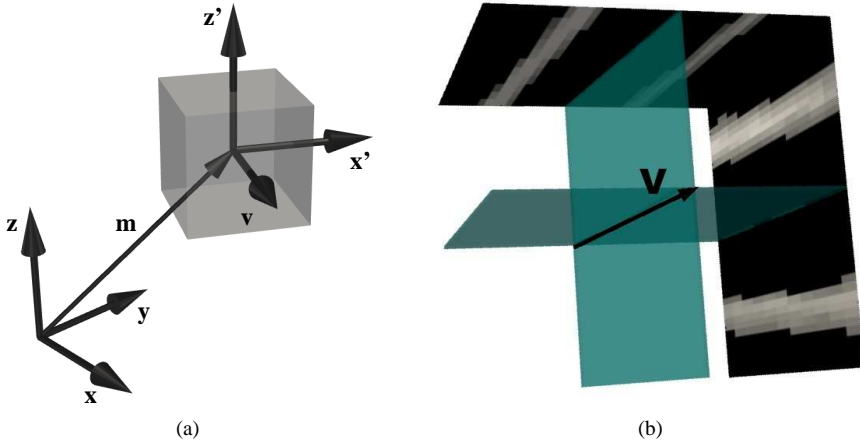


Figure 28: (a) The coordinate system used in the fibre tracking. (b) Illustration of the calculation of a new v direction using the intersection between two planes.

The fibre wall appears as two lines with higher intensity in each sum projected image. To obtain better images for further processing, the lowest intensities in the image are set to zero since they correspond to objects which only cover part of the volume. The fibre is assumed to cover most of the volume since only the volume inside the fibre wall is used for tracking. Figure 29(d–e) and (i–j) show the masked sum projections.

The sum projections are radon transformed to find the position and orientation of the fibre wall by identifying local maxima. Figure 30 shows the radon transforms of each of the masked sum projections in Figure 29. Each point in the radon transformed image corresponds to a line integral in the input image, which is the sum of all pixels along a ray in the image for a given angle, θ , and radius, r . The origin is located in the centre pixel of the image. The radon transform is pixel-wise normalised to remove the impact of shorter rays near the image edges. All rays equal or longer than the image size in the v direction are normalised by the length of each ray. For shorter rays the image size in the v direction is used for normalisation.

Local maxima are identified in the radon transformed images. If one local maximum can be found in each of the two halves, corresponding to the top and bottom part of the tracked fibre, a good estimate of the fibre wall locations and the next tracking position can be obtained from that projection. The maxima should be located approximately at the same angle. Some variation should be allowed if the fibre dimensions change. The radon transform radius that corresponds to the fibre dimensions should also be close to that calculated in previous tracking steps. In cases with multiple or missing maxima in each of the two halves, the existing maxima can be used to select maxima with information about fibre dimensions from previous tracking steps. Identified maxima from at least two of the projection images are needed to continue the tracking. If more than two projections have identified maxima the two best projections are selected. First projections with single maxima are used.

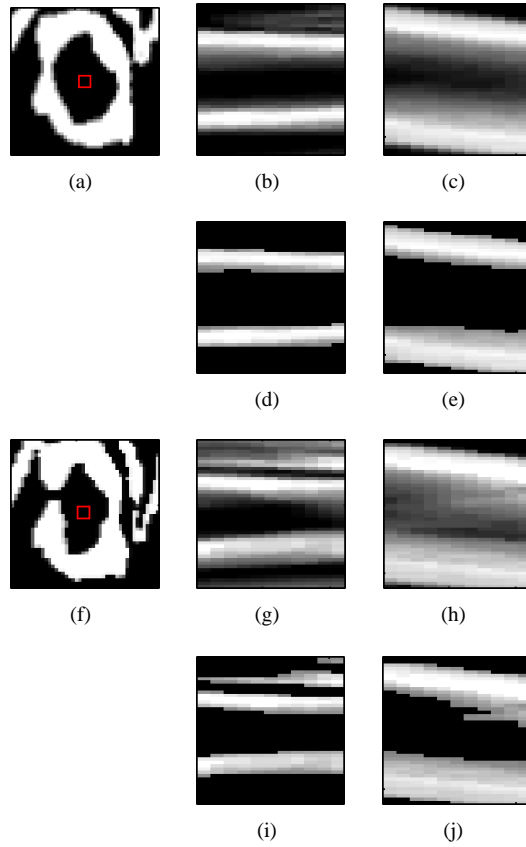


Figure 29: (a) Slice perpendicular to the \mathbf{v} direction at the current tracking position. (b–c) Sum projections of a local volume parallel to the rows and columns in (a). (d–e) Masked sum projections with lowest values set to zero. (f–j) Second example.

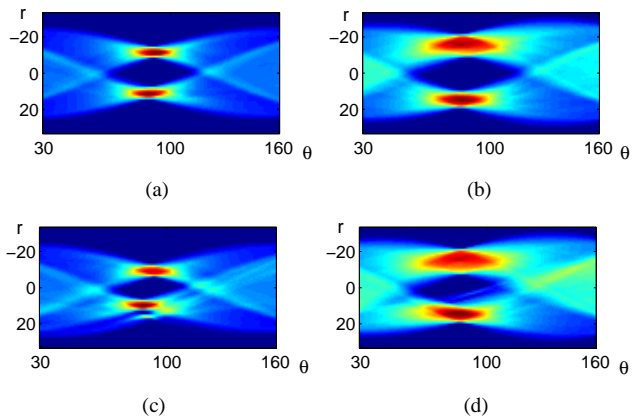


Figure 30: Radon transforms of the masked sum projections in Figure 29.

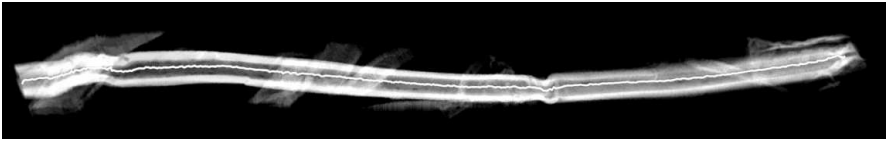
Estimates of the position and orientation of the fibre wall is calculated from each maximum in the projections. The current tracking point, \mathbf{m} , is corrected in the plane perpendicular to the fibre direction, \mathbf{v} , using the centre point between the two estimated fibre walls. This is the starting point for the next tracking step. A new estimate of \mathbf{v} is calculated by finding the mean orientation of the two fibre walls in each of the two projection images and finding the intersection between the two planes that these orientations describe in 3D together with the respective projection direction, see Figure 28(b). The tracking continues by taking a step L from the point \mathbf{m} in the new \mathbf{v} direction. The tracking ends if not enough maxima can be identified or the edge of the volume is hit.

In Paper V the method was evaluated on synchrotron X-ray microtomography images of wood fibre composite materials. Figure 13 shows a surface rendering of one of the materials. Good results are obtained for fibres with holes, cracks, irregular shape and partially collapsed fibres. See examples of the tracking results in Figure 31. These fibres are tracked through the main part of the volume image. Note that the tracking passes the collapsed part of the fibre in (a) without problems. The volumes used for the surface renderings in Figure 31(b), (d), and (f) are automatically extracted using information about the fibre cross sections from the tracking. This information can be used in complete segmentation and labelling of the fibre wall.

The method provides an approximation of the fibre centreline. In addition, the local fibre orientation and the fibre dimensions in each point are available for further segmentation steps or for estimation of the fibre orientation in the material. The sum projections are automatically adjusted to be approximately perpendicular to the local fibre direction. Problems with holes, cracks or partial collapse are handled implicitly. The tracking does not require the fibres to be aligned along the image coordinate axes as in the previously proposed methods. All fibres which fit the tubular fibre model can be tracked using the new approach. Completely collapsed fibres in binary images do not fit the model since no edges are visible. The method can be used both on binary data and on grey scale data with good contrast. Other types of input data may also be used to track fibres. Examples that have been tested include fuzzy input or distance transformed fibres of almost completely collapsed fibres where the distance values are used to enhance the tubular structure. The method can also be adapted to tubular structures in other applications, such as volume images of blood vessels.

In future work the result from the method can be used as input to full fibre segmentation with labelling of individual fibres. One possible way is to use region growing to label the voxels that belong to the closest fibre. In addition, the information about the location of the fibre wall may be used to obtain better fibre segmentation. It is also left for future work to add an automatic seeding step. Possible starting points can be evaluated automatically to test if they are inside the fibre lumen.

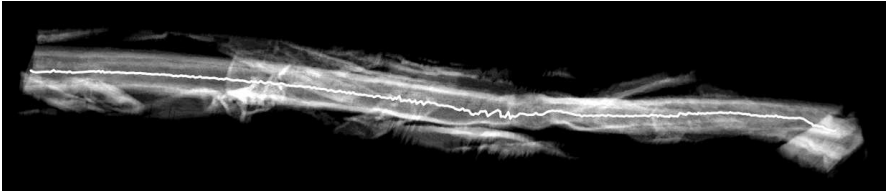
The success of methods for segmentation and labelling of individual fibres in volume images will strongly depend on the material properties. If the fibres can be individually segmented manually, it will be possible to find a method for automatic



(a)



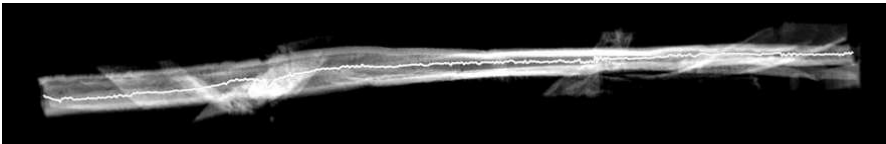
(b)



(c)



(d)



(e)



(f)

Figure 31: Tracking results for three individual fibres. (a) Tracking result for the first fibre overlaid on a sum projection of a subvolume defined by the tracking parameters. (b) Surface rendering of the subvolume in (a). (c–d) Tracking result for the second fibre. (e–f) Tracking result for the third fibre.

segmentation. If it is hard to determine if a given part belongs to a certain fibre or not, it will be a difficult problem to automate. Also, some paper grades will be easier to segment than others, such as materials with less collapsed and cracked fibres, less fine material, and less fibres per volume. Different approaches for fibre segmentation may be successful for different paper grades and different types of fibre-based materials.

7 Fibre orientation estimation

Fibre orientation is an important structural property of fibre-based materials. In paper, the fibre orientation is determined by the flow of the suspension when the fibre web is formed on the wire screen. The fibre orientation affects physical properties such as strength, stiffness, elasticity, and hygroexpansion. For example, if the fibre orientation is different on the top and bottom side of the sheet, moisture changes makes the sheet curl or twist during printing.

Fibre orientation is not measured online in paper manufacturing. Offline, it is common to estimate the fibre orientation in 2D using both indirect methods, such as light scattering, and direct methods, such as sheet splitting (Erkkilä et al., 1998). Sheet splitting has been further developed and is now the predominant direct method for analysing fibre orientation in paper. A summary of sheet splitting methods can be found in Hirn and Bauer (2007). In sheet splitting, the sheet is divided into layers parallel to the plane of the sheet by hand after lamination using a heat seal laminator. The layers of the sheet are scanned in a flat bed scanner and the fibre orientation is measured using gradient image analysis. It is common to analyse A4 or A3 sheet sizes with an orientation estimate for each 2×2 mm. This gives an overview of the fibre orientation. However, the method only provides large scale estimates and the out-of-plane orientation can not be measured.

More knowledge about the 3D structure can be gained by analysing the 3D fibre orientation in volume images. For fibre-based materials with straight regularly shaped fibres, such as some synthetic fibres, stereological methods can be applied. This type of methods is not suitable for natural fibres, such as wood fibres, due to the large natural variability and large deformations of the fibres in the paper making process. A direct 3D method for fibres in volume images was proposed by Robb et al. (2007). They used anisotropic Gaussian filters with varying orientation. However, as the orientation estimate is given by the orientation of the filter with the largest response, many filters are needed to obtain good angular resolution in 3D.

In Paper VI, a new method for estimating 3D fibre orientation in volume images is presented. The method can be applied directly to grey scale volume images and does not require a segmentation of fibre and void. The result is an orientation estimate for each voxel neighbourhood, which provides estimates of the 3D fibre orientation and fibre orientation anisotropy for parts of or the whole sheet. In contrast to previous methods, any orientation in 3D can be estimated. The method is demonstrated on a wood fibre composite material. In Paper VII scale and noise sensitivity of the presented method is investigated for both tubular and solid fibres and the method is demonstrated on a volume image of press felt. In addition, a method for selecting scale using an estimate of the fibre radius in each voxel is presented for solid fibres.

The fibre orientation in a material is assumed to correlate directly with the local signal orientation in the image. There are different approaches for estimation of local orientation using structure tensors (Kass and Witkin, 1987; Bigun and Granlund, 1987; Bigun et al., 1991; Granlund and Knutsson, 1995). Here, the framework for

local orientation estimation described in Granlund and Knutsson (1995) is used, but the other approaches are expected to provide similar results.

At least six evenly spread phase invariant quadrature filters are needed for estimating local orientation in 3D (Granlund and Knutsson, 1995). The centre frequency of the radial part of the filters is selected to correspond to the size of the edges of the fibres. The input image is convolved with the filters and a structure tensor is calculated from the filter responses. The structure tensor can be represented by a 3×3 symmetric matrix. The tensor field is smoothed using a small Gaussian mask for each of the six independent component images. This reduces local errors and improves the fibre orientation estimate. The fibre orientation is assumed to vary slower than the small scale variations that are suppressed by the smoothing.

The local orientation and the local structure anisotropy in a voxel neighbourhood can be obtained from the eigenvalues and eigenvectors of the structure tensor. The eigenvalues of the tensor are sorted in descending order. The sorted eigenvalues are denoted λ_1 , λ_2 , and λ_3 and the corresponding eigenvectors are denoted \mathbf{e}_1 , \mathbf{e}_2 , and \mathbf{e}_3 . The relative tensor anisotropy can be calculated from the eigenvalues as

$$c_1 = \frac{\lambda_1 - \lambda_2}{\lambda_1}, \quad c_2 = \frac{\lambda_2 - \lambda_3}{\lambda_1}, \quad c_3 = \frac{\lambda_3}{\lambda_1} \quad (5)$$

The fibre orientation is estimated as the local orientation with the least signal variation, which is described by the eigenvector \mathbf{e}_3 . A certainty estimate for the estimated orientation is provided by the c_2 value from the relative tensor anisotropy. c_2 is large in neighbourhoods where the eigenvalues λ_1 and λ_2 are large and λ_3 is small. This corresponds to a case where there are large signal variations in the \mathbf{e}_1 and \mathbf{e}_2 orientations, relative to the \mathbf{e}_3 orientation. If c_2 is small, the signal variation can either have one main orientation, indicated by a large c_1 value, or be almost equal in all three orientations, indicated by a large c_3 value.

The method provides an orientation estimate with a corresponding certainty measurement for each voxel neighbourhood. The estimates can be averaged for parts of or the whole sample depending on the desired output. In particular, averaging can be used to evaluate the orientation in different layers of a paper sheet. The 3D distribution of fibre orientation and the corresponding orientation anisotropy can be calculated from the estimated orientations. Anisotropy is calculated using the sum of outer products of the orientation estimates. The ratios between the eigenvalues of the resulting matrix describe the anisotropy of the fibre orientation. When calculating anisotropy and fibre orientation distributions the certainty estimate c_2 is used as weights for the estimates. The image intensity or a mapping of the intensity is also used to only include voxels that contain fibres in the measurement.

The presented method has been evaluated using synthetic volume images with known fibre orientation. The mean error for the estimation is calculated as

$$E_n = \frac{\sum_I w c_2 \arccos(|\mathbf{v}_{\text{gt}} \cdot \mathbf{e}_3|)}{\sum_I w c_2} \quad (6)$$

where w is a weight based on the image intensity, c_2 is the certainty value, \mathbf{v}_{gt} is the ground truth orientation, and \mathbf{e}_3 is the estimated orientation.

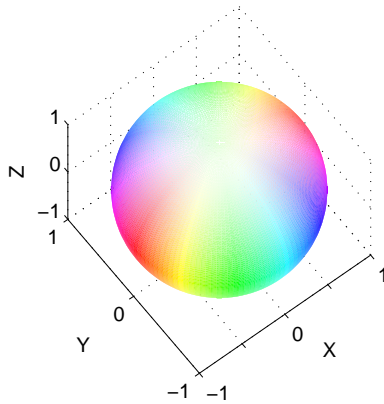


Figure 32: Colour map for the estimated orientations. Hue varies with the X and Y coordinates and saturation with the Z coordinate.

In Paper VI the method is evaluated using a test set with straight tubular fibres. The evaluation shows that smoothing the tensor field prior to calculation of the eigenvalues and eigenvectors decreases the estimation error. It is also shown that the estimation error can be further decreased by weighing each estimate with the corresponding certainty value. The largest errors occur close to the fibre ends where the signal variation may not be smallest in the true fibre orientation.

In Paper VII the method is further evaluated using a larger test set and the sensitivity to scale and noise is investigated. Synthetic test volumes with either solid or tubular fibres were generated. Two volumes with the same positions and orientations for the fibres were used for the two cases. Six different fibre diameters were investigated. These correspond to different fibre dimensions in the same volume or different resolutions of the volume. Ten volumes for each fibre dimension were used in the test set to obtain good statistics. Gaussian noise was also added to the test images. The evaluation shows that the presented method is applicable to both tubular and solid fibres. The error is generally larger for solid fibres of the same diameter as the tubular fibres, except for the smallest fibre diameters. The evaluation also shows that the method is robust to noise and performs well at different scales. The results can be used as a guide to select scale and parameters when the method is applied to real data.

Figure 33 shows volume renderings of a part of a synthetic volume for both the ground truth estimates and the estimated orientations. The fibres are coloured according to the orientation vector in each voxel using the colour map presented in Paper VI. The colour map is illustrated in Figure 32. Hue varies with the X and Y coordinates and saturation varies with the Z coordinate. This colour map is suitable for highly layered materials such as paper. As can be seen in Figure 33 there is good correspondence between the ground truth orientations and the estimated orientations. Figure 34 shows the fibre orientation distribution for the ground truth and the orientation estimates projected on the YZ and ZX planes for the synthetic test image in Figure 33.

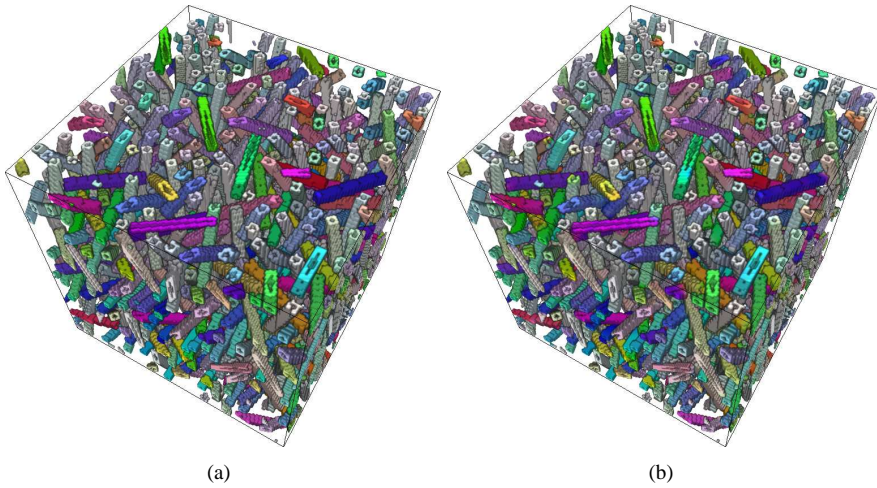


Figure 33: Volume renderings of the fibre orientations in a part of a synthetic test image. (a) Ground truth orientations. (b) Estimated 3D fibre orientations.

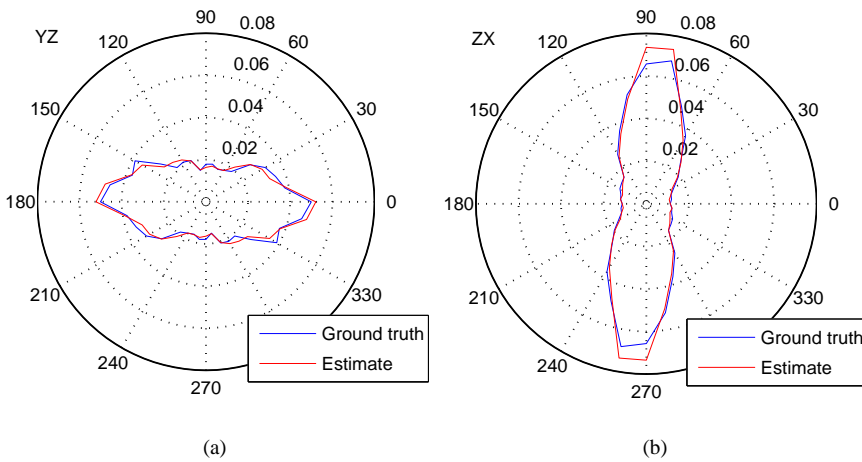
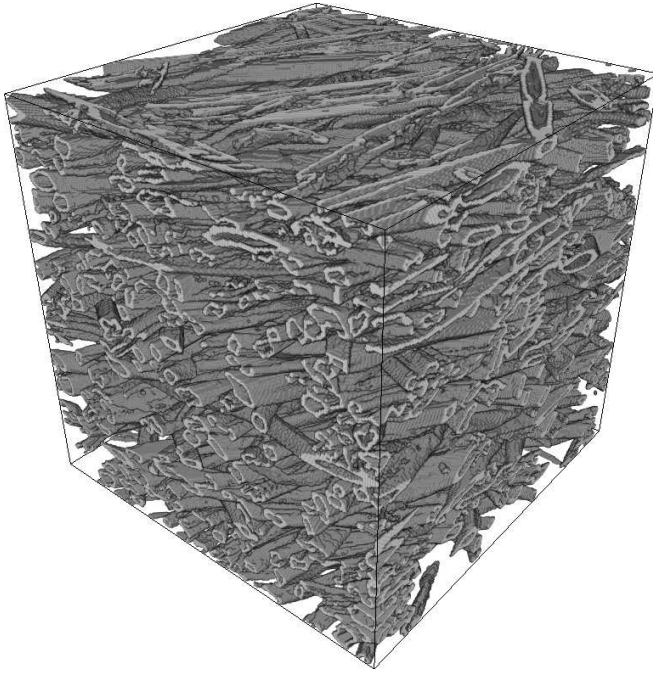
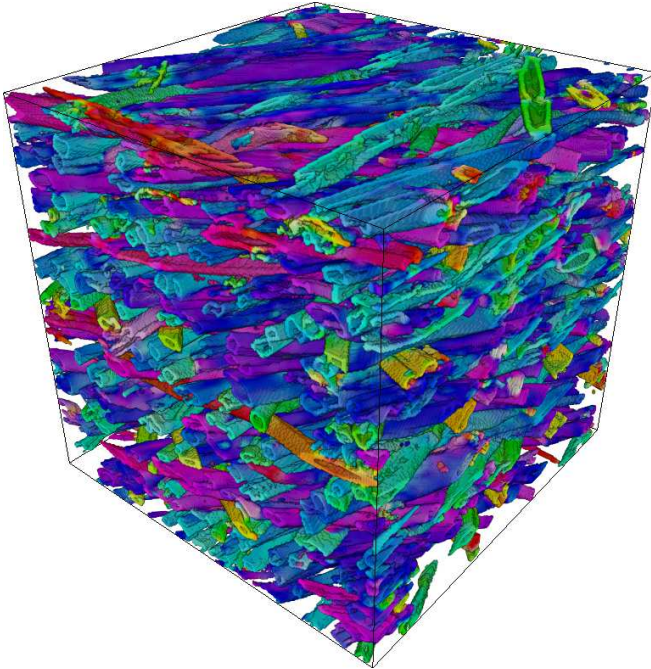


Figure 34: (a) Fibre orientation distribution in the YZ plane. (b) Fibre orientation distribution in the ZX plane.

In Paper VI the method is evaluated using synchrotron X-ray microtomography images of wood fibre composites and paper and appears to provide good results. Figure 35 shows volume renderings of the fibre network and the estimated orientations in a wood fibre composite material. The matrix is made transparent to show the fibres in the material. In Paper VII the method is demonstrated on a desktop X-ray microtomography image of press felt. Figure 36 shows volume renderings of the fibre network and the estimated orientations in the felt. The orientation of the fibres in the base weave is not estimated.

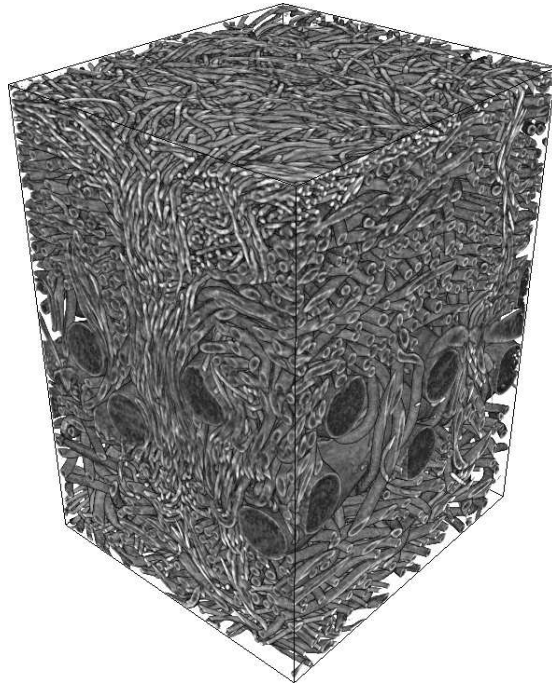


(a)

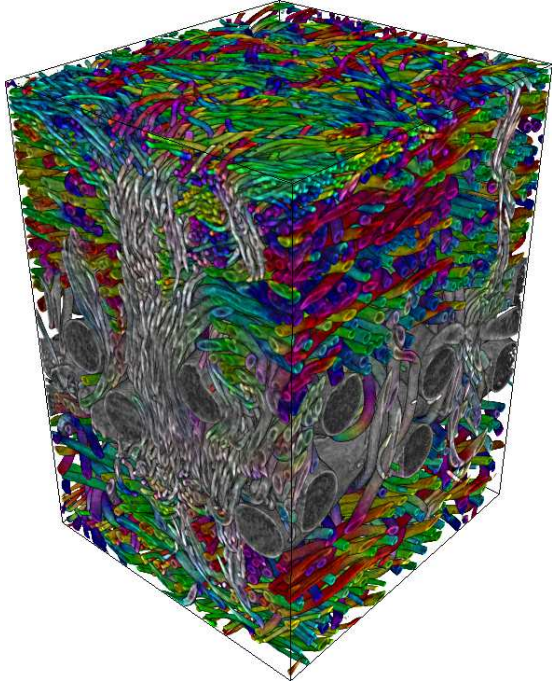


(b)

Figure 35: (a) Volume rendering of the fibres in a wood fibre composite material. (b) Estimated fibre orientations.



(a)



(b)

Figure 36: (a) Volume rendering of the fibres in a press felt. (b) Estimated fibre orientations.

Paper VII also presents a new method for weighting estimates from different parameter setups for volume images with solid fibres of different diameters. A segmented image, where each voxel contains the approximate fibre radius, is obtained using a binary image of the fibres. The image is binarised using bilateral filtering (Tomasi and Manduchi, 1998) and hysteresis thresholding (Canny, 1986). The fibres are distance transformed (Borgefors, 1996) and the watershed algorithm (Vincent and Soille, 1991) is applied to the distance transform. The distance transform is smoothed to reduce the number of regions that are caused by small shape variations and noise. Regions from the watershed are labelled with the corresponding distance maximum in the distance transform. This gives a weight image, which is suitable to use in analysis of solid fibres. In Paper VII it is demonstrated how the weight image can be used to select orientation estimates from three results obtained using different parameter setups. In addition to weighting estimates the segmentation provides an approximate distribution of the fibre dimensions.

The results in Paper VI and Paper VII show that 3D fibre orientation can be well estimated using the presented method. The method is applicable to both tubular and solid fibres, such as wood fibres and synthetic fibres. It can be used directly in grey scale images without initial segmentation of fibre and void. All orientations in 3D can be estimated with good accuracy using six quadrature filters. A certainty measurement is available for each orientation estimate and weighting the orientation estimates by the certainty estimates improves the results.

The results indicate that it is possible to use lower resolution of the volume images when measuring orientation than for other measurements. Larger physical size of the samples can be imaged and the resolution obtained using desktop X-ray microtomography scanners is sufficient to estimate 3D fibre orientation.

With the presented method it is possible to estimate the out-of-plane orientation of fibres. This is not possible using for example sheet splitting. The method can also be used to estimate the 2D fibre orientation in images from, for example, sheet splitting to obtain increased spatial resolution of the 2D estimates. This needs to be further investigated in future studies. Another topic for future work is further investigation of possibilities for automatic scale selection to decrease the overall estimation error. This may be particularly interesting for materials with different fibre dimensions such as press felts.

8 Conclusion and future work

In this chapter, the contributions of this thesis are summarised and suggestions for future work are given.

8.1 Summary of contributions

The main contributions of this thesis are image analysis methods for analysing the microstructure of fibre-based materials in volume images. Another contribution of this work is a general method for ring artifact reduction.

Several methods for analysing the microstructure of fibre-based materials have been presented. All methods have been developed with the aim to utilise the full 3D information in the volume images. In addition, they have been developed to be applicable to volume images from different modalities and with different resolutions. The methods have been designed for characterisation of fibre-based materials based on both wood fibres and synthetic fibres. They have also been designed to be general and are intended for use also in other fields where automated image analysis is used as a tool for structure characterisation.

A method for reducing ring artifacts in high resolution X-ray microtomography images has been developed. The method has been evaluated on real images and has been shown to provide good reduction performance for both full and partial rings. It has been used as a preprocessing step before the other methods presented in this thesis have been applied to the X-ray microtomography images. The method is general and is expected to provide artifact reduction also in images acquired using other tomography systems than synchrotron X-ray microtomography.

A number of methods for characterising pores in volume images have been developed, both for pores in paper and pores in press felts. A work flow for analysing the pore structure in volume images of paper and two new pore structure representations with corresponding measurements have been presented. The methods have been applied to real paper samples to show their suitability for pore structure characterisation. For press felts, a method to estimate the interface pore volume between paper web and press felt has been developed. The method has been used in a case study with four press felts.

Two methods for analysing fibres and the fibre network in volume images have been presented. One of these methods tracks individual fibres, by estimating the fibre centreline, the local fibre orientation, and the fibre dimensions. In an evaluation using real data the method provided good tracking results for different fibre shapes, even for almost collapsed fibres and fibres with irregular shape. The other method estimates 3D fibre orientation in volume images. This method estimates the fibre orientation directly in grey scale images and does not require an initial segmentation of individual fibres. The estimation error for different scales and noise levels has been studied using synthetic data. The method has proven applicable to both tubular and solid fibres, such as wood fibres and synthetic fibres. The method has also been evaluated in experiments on real data where it appears to provide good results.

8.2 Future work

All presented methods have been evaluated using real data with good results. However, larger studies of materials with known properties would provide better insight into the applicability of the presented methods to different problem settings. The image material needed for such studies is large and the available beam time at synchrotron facilities is limited. Volume images from desktop X-ray microtomography scanners may be used instead, since the availability of scanners with sufficient resolution is increasing.

In addition to large scale evaluation of the presented methods using real data, further development of methods for structure characterisation is needed. There are many interesting paths to follow for future work. One of the main goals in image analysis of material microstructure is completely automated analysis of volume images. For fibre-based materials this may be enabled by a complete segmentation of individual fibres. Fibre tracking and fibre segmentation methods, such as the fibre tracking method presented here, is a possible path to follow for future work in this area. A suggested addition to the presented method is automated seeding of the fibres using, for example, lumen segmentation. The focus of further developments in this field should also lie on development of 3D methods for segmentation, to make use of the information that is available in volume images.

Another approach is to follow the path where measurements of the structure can be obtained without segmentation of individual fibres. Since material properties often depend on the average properties of the subparts, it may be possible to estimate many important properties well enough using local low-level measurements. One such measurement presented here is the 3D fibre orientation estimation. Other measurements that may be obtained in this way are local material density and size distributions. Area estimates may also be interesting to study in this way. Two examples are the area of the fibre-void interface in paper and the fibre-matrix interface in wood fibre composites.

Also for pore structure characterisation there are future paths to follow. Investigation of the pore structure in press felts using volume images is an interesting topic where the methods for pore structure characterisation of paper can be applied. It is also left for future work to investigate the applicability of the pore structure representations to other porous materials or to characterisation of other hollow structures.

References

- Antoine, C., Nygård, P., Gregersen, Ø. W., Holmstad, R., Weitkamp, T., and Rau, C. (2002). 3D images of paper obtained by phase-contrast X-ray microtomography: Image quality and binarisation. *Nuclear Instruments and Methods in Physics Research, Section A: Accelerators, Spectrometers, Detectors and Associated Equipment*, 490(1–2):392–402.
- Aronsson, M. (2002a). Estimating Fibre Twist and Aspect Ratios in 3D Voxel Volumes. In *Proceedings of ICPR*, Québec, Canada. IEEE.
- Aronsson, M. (2002b). *On 3D Fibre Measurements of Digitized Paper - from Microscopy to Fibre Network*. Silvestria 254, Swedish University of Agricultural Sciences, Uppsala.
- Aronsson, M. and Borgefors, G. (2001). 2D segmentation and labelling of clustered ring shaped objects. In *Proceedings Scandinavian Conference on Image Analysis (SCIA)*, pages 272–279.
- Aronsson, M., Henningsson, O., and Sävborg, O. (2002). Slice-based Digital Volume Assembly of a Small Paper Sample. *Nordic Pulp and Paper Research journal*, 17(1):29–33.
- Aronsson, M. and Sintorn, I.-M. (2002). Ring Shaped Object Detector for Non-isotropic 2D Images using Optimized Distance Transform Weights. In *International Conference on Image Processing (ICIP)*, pages 985–988.
- Bache-Wiig, J. and Henden, P.-C. (2005). Individual fiber segmentation of three-dimensional microtomograms of paper and fiber-reinforced composite materials. Master's thesis, Department of Computer and Information Science, Norwegian University of Science and Technology.
- Baldwin, C., Sederman, A., Mantle, M., Alexander, P., and Gladden, L. (1996). Determination and characterization of the structure of a pore space from 3D volume images. *Journal of Colloid and Interface Science*, 181:79–92.
- Beucher, S. and Lantuéjoul, C. (1979). Use of watersheds in contour detection. In *International Workshop on Image Processing: Real-time and Motion Detection/Estimation*, pages 2.1–2.12.
- Bigun, J. and Granlund, G. (1987). Optimal orientation detection of linear symmetry. In *First International Conference on Computer Vision, ICCV*, pages 433–438, London. IEEE Computer Society.
- Bigun, J., Granlund, G. H., and Wiklund, J. (1991). Multidimensional orientation estimation with applications to texture analysis and optical flow. *IEEE Transactions on Pattern Analysis and Machine Intelligence*, 13(8):775–790.
- Borgefors, G. (1996). On Digital Distance Transforms in Three Dimensions. *Computer Vision and Image Understanding*, 64(3):368–376.

- Bracewell, R. and Riddle, A. (1967). Inversion of fan beam scans in radio astronomy. *Astrophysics Journal*, 150:427–434.
- Canny, J. F. (1986). A computational approach to edge detection. *IEEE Transactions on Pattern Analysis and Machine Intelligence*, 8(6):679–698.
- Chinga, G., Axelsson, M., Eriksen, O., and Svensson, S. (2008). Structural characteristics of pore networks affecting print-through. *Journal of Pulp and Paper Science*, 34(1):13–22.
- Chinga, G., Johnsen, P., and Diserud, O. (2004). Controlled serial grinding for high-resolution three-dimensional reconstruction. *Journal of Microscopy*, 214(1):13–21.
- Cloetens, P. (1999). *Contribution to Phase Contrast Imaging, Reconstruction and Tomography with Hard Synchrotron Radiation – Principles, Implementation and Applications*. PhD thesis, Vrije Universiteit Brussel.
- Dickson, A. R. (2000). Quantitative analysis of paper cross-sections. *Appita Journal*, 53(4):292–295.
- Donoser, M. and Bischof, H. (2006). Efficient Maximally Stable Extremal Region (MSER) Tracking. In *IEEE Computer Society Conference on Computer Vision and Pattern Recognition (CVPR)*, pages 553–560.
- Donoser, M., Mauthner, T., Bischof, H., and Kritzinger, J. (2008). A Probabilistic Approach For Tracking Fibers. In *International Conference on Pattern Recognition (ICPR 2008)*.
- Erkkilä, A.-L., Pakarinen, P., and Odell, M. (1998). Sheet forming studies using layered orientation analysis. *Pulp and Paper Canada*, 99(1):81–85.
- Fransson, D. (2007). Noise reduction of X-ray microtomography images of paper using anisotropic filtering methods. Master’s thesis, Centre for Image Analysis, Uppsala University.
- Goel, A., Arns, C., Holmstad, R., Gregersen, O., Bauget, F., Averdunk, H., Sok, R., Sheppard, A., and Knackstedt, M. (2006). Analysis of the impact of papermaking variables on the structure and transport properties of paper samples by X-ray microtomography. *Journal of pulp and paper science*, 32(3).
- Goel, A., Tzanakakis, M., Huang, S., Ramaswamy, S., Choi, D., and Ramaro, B. (2001). Characterization of three-dimensional structure of paper using X-ray microtomography. *Tappi Journal*, 84(5):72.
- Granlund, G. H. and Knutsson, H. (1995). *Signal Processing for Computer Vision*. Kluwer Academic Publishers. ISBN 0-7923-9530-1.
- Hasuike, M., Kawasaki, T., and Murakami, K. (1992). Evaluation Method of 3-D Geometric Structure of Paper Sheet. *Journal of Pulp and Paper Science*, 18(3):114–120.

- Hirn, U. and Bauer, W. (2007). Evaluating an improved method to determine layered fibre orientation by sheet splitting. In *61st Appita Annual Conference and Exhibition, Gold Coast, Australia 6-9 May 2007*, pages 71–79.
- Holen, R. and Hagen, M. (2004). Segmentation of absorption mode X-ray micro tomographic images of paper. Master's thesis, Department of Computer and Information Science, Norwegian University of Science and Technology.
- Holmstad, R., Goel, A., Ramaswamy, S., and Gregersen, O. (2006). Visualization and characterization of high resolution 3D images of paper samples. *Appita Journal*, 59(5):370–390.
- Holmstad, R., Gregersen, O., Aaltosalmi, U., Kataja, M., Koponen, A., Goel, A., and Ramaswamy, S. (2005). Comparison of 3D structural characteristics of high and low resolution X-ray microtomographic images of paper. *Nordic Pulp and Paper Research Journal*, 20(3):283–288.
- Huang, S., Goel, A., Ramaswamy, S., Ramarao, B. V., and Choi, D. (2002). Transverse and in-plane pore structure characterisation of paper. *Appita Journal*, 55(3):230–234.
- Jennesson, P., Gilboy, W., E.J. M., and P.J., G. (2003). An X-ray micro-tomography system optimised for the low-dose study of living organisms. *Applied Radiation and Isotopes*, 58:177–181.
- Kass, M. and Witkin, A. (1987). Analyzing Oriented Patterns. *Computer Vision, Graphics, and Image Processing*, 37:362–385.
- Knutsson, H. and Westin, C.-F. (1993). Normalized and differential convolution: Methods for interpolation and filtering of incomplete and uncertain data. In *Proceedings of IEEE Computer Society Conference on Computer Vision and Pattern Recognition*, pages 515–523.
- Landis, H. (2002). *Production-ready global illumination, July 2002. Course 16: RenderMan in Production. ACM SIGGRAPH 2002 Course Notes*. ACM, Boston.
- Lindquist, W., Lee, S.-M., Coker, D., Jones, K., and Spanne, P. (1996). Medial axis analysis of void structure in three-dimensional tomographic images of porous media. *Journal of Geophysical Research*, 101(B4):8297–8310.
- Lindquist, W. and Venkatarangan, A. (1999). Investigating 3D geometry of porous media from high resolution images. *Physics and Chemistry of the Earth, Part A: Solid Earth and Geodesy*, 25(7):593–599.
- Lorensen, W. and Cline, H. (1987). Marching cubes: A high resolution 3D surface construction algorithm. In *Proceedings of SIGGRAPH '87*, volume 21, pages 163–169.
- Malmberg, F. (2008). *Segmentation and Analysis of Volume Images, with Applications*. Licentiate thesis, Swedish University of Agricultural Sciences.

- Moss, P., Retulainen, E., Paulapuro, H., and Aaltonen, P. (1993). Taking a new look at pulp and paper: Applications of confocal laser scanning microscopy (CLSM) to pulp and paper research. *Paper and Timber*, 75(1–2):74–79.
- Perona, P. and Malik, J. (1990). Scale-space and edge detection using anisotropic diffusion. *Pattern Analysis and Machine Intelligence*, 12(7):629–639.
- Piper, J. and Granum, E. (1987). Computing distance transformations in convex and non-convex domains. *Pattern Recognition*, 20(6):599–615.
- Ramaswamy, S., Gupta, M., Goel, A., Aaltosalmi, U., Kataja, M., Koponen, A., and Ramarao, B. (2004). The 3D structure of fabric and its relationship to liquid and vapor transport. *Colloids and Surfaces A: Physicochem. Eng. Aspects*, 241:323–333.
- Ramaswamy, S., Huang, S., Goel, A., Cooper, A., Choi, D., Bandyopadhyay, A., and Ramarao, B. (2001). The 3D structure of paper and its relationship to moisture transport in liquid and vapor forms. In *The science of papermaking – 12th Fundamental research symposium*, volume 2, pages 1289–1311, Oxford, UK.
- Raven, C. (1998). Numerical removal of ring artifacts in microtomography. *Review of Scientific instruments*, 69(8):2978–2980.
- Robb, K., Wirjandi, O., and Schladitz, K. (2007). Fiber orientation estimation from 3D image data: Practical algorithms, visualization, and interpretation. In *Proceedings of 7th International Conference on Hybrid Intelligent Systems*, pages 320–325.
- Rolland du Roscoat, S., Bloch, J.-F., and Thibault, X. (2005a). 3D paper structure with X-ray synchrotron radiation microtomography. In *13th Fundamental Research Symposium, Cambridge*, pages 901–920.
- Rolland du Roscoat, S., Bloch, J.-F., and Thibault, X. (2005b). Synchrotron radiation microtomography applied to investigation of paper. *Journal of Physics D: Applied physics*, 38(10A):78–84.
- Samuelsen, E., Gregersen, Ø. W., Houen, P.-J., Helle, T., Raven, C., and Snigirev, A. (2001). Three-Dimensional Imaging of Paper by Use of Synchrotron X-Ray Microtomography. *Journal of Pulp and Paper Science*, 27(2):50–53.
- Sijbers, J. and Postnov, A. (2004). Reduction of ring artefacts in high resolution micro-CT reconstructions. *Physics in Medicine and Biology*, 49(14):N247–N253.
- Sintorn, I.-M. and Borgefors, G. (2004). Weighted distance transforms for volume images digitized in elongated voxel grids. *Pattern Recognition Letters*, 25(5):525–601. Special Issue on Discrete Geometry for Computer Imagery (DGCI’2002).
- Smith, S. and Brady, J. (1997). SUSAN - a new approach to low level image processing. *International Journal of Computer Vision*, 23(1):45–78.
- Sternberg, S. (1983). Biomedical image processing. *IEEE Computer*, 16(1):22–34.

- Svensson, S. and Aronsson, M. (2001). Some measurements of fibres in volume images of paper using medial representations detected on distance transforms. In *2001 IEEE Computer Society Conference on Computer Vision and Pattern Recognition (technical sketches)*, volume 2 (CD-ROM), Kauai, Hawaii.
- Svensson, S. and Aronsson, M. (2003). Using distance transform based algorithms for extracting measures of the fibre network in volume images of paper. *IEEE transaction on systems man and cybernetics part B - Cybernetics*, 33(4):562–571.
- Tang, X., Ning, R., Yu, R., and Conover, D. (2001). Cone beam volume CT image artifacts caused by defective cells in x-ray flat panel imagers and the artifact removal using a wavelet-analysis-based algorithm. *Medical Physics*, 28(5):812–825.
- Thibault, X., Bloch, J.-F., and Boller, E. (2002). Felt structure characterised by synchrotron microtomography. *Appita Journal*, 55(2):145–148.
- Tomasi, C. and Manduchi, R. (1998). Bilateral filtering for gray and color images. In *IEEE International Conference on Computer Vision '98*, pages 836–846.
- Turpeinen, T., Svensson, S., Östlund, C., Hyväluoma, J., and Timonen, J. (2008). Using image analysis to model 3D liquid-paper interaction. In *Proceedings of Progress in Paper Physics Seminar 2008*, pages 79–82.
- Vidal, F. P., Letang, J. M., Peix, G., and Cloetens, P. (2005). Investigation of artefact sources in synchrotron microtomography via virtual X-ray imaging. *Nuclear Instruments and Methods in Physics Research B*, 234:333–348.
- Vincent, L. and Soille, P. (1991). Watersheds in digital spaces: An efficient algorithm based on immersion simulations. *IEEE Transactions on Pattern Analysis and Machine Intelligence*, 13(6):583–598.
- Walbaum, H. and Zak, H. (1976). Internal structure of paper and coatings in SEM cross-sections. *TAPPI Journal*, 59(3):102–105.
- Walther, T., Terzic, K., Donath, T., Meine, H., Beckmann, F., and Thoemen, H. (2006). Microstructural analysis of lignocellulosic fiber networks. In Bonse and Ulrich, editors, *Developments in X-Ray Tomography V. Proceedings of the SPIE.*, volume 6318.
- Wiltsche, M. (2005). *Three Dimensional Analysis of Paper Structure Using Automated Microtomy*. PhD thesis, Graz University of Technology.

Related work

In addition to the papers included in this thesis, the author has also contributed to the following publications:

Reviewed publications

Chinga, G., Axelsson, M., Eriksen Ø, and Svensson, S. (2008). Structural Characteristics of Pore Networks Affecting Print-Through. *Journal of Pulp and Paper Science*, 34(1):13–22.

Non-reviewed publications

Axelsson, M. (2008). Tracking Tubular Structures in Volume Image Data. In *Proceedings SSBA 2008, Symposium on image analysis, Lund*.

Axelsson, M., Svensson, S., and Borgefors, G. (2007). 2D Ring Artifact Reduction of X-ray Tomography Images. In *Proceedings SSBA 2007, Symposium on image analysis, Linköping*.

Axelsson, M., Chinga, C., Svensson, S., Nygård, P., Malmberg, F., Solheim, O., Lindblad, L., and Borgefors, G. (2006). Detailed quantification of the 3D structure of newsprints in X-ray synchrotron radiation microtomography images. In *Progress in Paper Physics Seminar, Oxford, Ohio, USA*.

Bogren, K., Gamstedt, K., Berthold, F., Lindström, M., Nygård, P., Malmberg, F., Lindblad, J., Axelsson, M., Svensson, S., and Borgefors, G. (2006). Stress transfer and failure in pulpfibre reinforced composites: Effects of microstructure characterized by X-ray microtomography. In *Progress in Paper Physics Seminar, Oxford, Ohio, USA*.

Nygård, P., Gradin, P., Gregersen, Ø., Lindblad, J., Axelsson, M., Svensson, S., Malmberg, F., and Borgefors, G. (2006). Damage Mechanisms in Paper. *Progress in Paper Physics Seminar, Oxford, Ohio, USA*.

Axelsson, M., Östlund, C., Vomhoff, H., and Svensson, S. (2006). Volume estimation of the interface pores between paper web and press felt. In *Proceedings SSBA 2006, Symposium on image analysis, Umeå*.

Axelsson, M., Sintorn, I.-M., Svensson, S., and Borgefors, G. (2005). Individual pore segmentation in 3D volumes of fibrous materials. In *Proceedings SSBA 2005, Symposium on image analysis, Malmö*.

Acknowledgments

The work in this thesis was performed at the Centre for Image Analysis in Uppsala between June 2004 and February 2009. I want to thank everyone who has supported me during this time. Special thanks to:

- ▷ My supervisors Prof. Gunilla Borgefors and Doc. Stina Svensson for advice and support.
- ▷ All collaboration partners and external co-authors: Catherine Östlund, Hannes Vomhoff, Marco Lucisano, Karin Almgren, and Kristofer Gamstedt at STFI-Packforsk in Stockholm. Per Nygård and Gary Chinga at PFI in Trondheim. Especially Per Nygård for starting a collaboration with CBA, in which I got the opportunity to work with X-ray microtomography images. Örjan Sävborg and Olle Henningsson at Stora Enso in Falun.
- ▷ All researchers whom I have met during this time who have shared their knowledge and given input on my work.
- ▷ The past and present members of the fibre research group at CBA: Gunilla Borgefors, Stina Svensson, Ida-Maria Sintorn, Filip Malmberg, Joakim Lindblad, Bettina Selig, Cris Luengo, Erik Wernersson, Anders Brun, and our guest researcher Catherine Östlund.
- ▷ Everyhopa at CBA. Both past and present employees have made the time at CBA great. In particular, I want to thank Bettina Selig and Lennart Svensson for being especially helpful and Kristin Norell for always taking time to discuss all types of research problems.
- ▷ Gunilla Borgefors, Cris Luengo, Joakim Rydell, Anders Nilsson, Stina Svensson, and Bo Nilsson for proofreading the thesis.
- ♡ My best friend Joakim for his advice and valuable comments on many parts of my work. Ideas always improve when they are discussed and examined. Also, thank you for great friendship!
- ♡ My family for their constant love and support.
- ♡ All my friends and relatives.
- ♡ Anders for his constant love, care, and support. Thank you for your help during this time. Jag älskar dig!
- ♪ All members of The Gloryfires. I send you my warmest thanks and gratitude for the times we have shared. It has been a great joy both to practice and perform with you.

Uppsala, February 2009
Maria Axelsson